

Energy losses and transition radiation produced by the interaction of charged particles with a graphene sheet

Zoran L. Mišković,¹ Silvina Segui,^{2,*†} Juana L. Gervasoni,^{2,3,†} and Néstor R. Arista^{2,3}

¹*Department of Applied Mathematics, and Waterloo Institute for Nanotechnology, University of Waterloo, Waterloo, Ontario, Canada N2L 3G1*

²*Centro Atómico Bariloche, Comisión Nacional de Energía Atómica, Av. Bustillo 9500, 8400 S.C. de Bariloche, Argentina*

³*Instituto Balseiro, Universidad Nacional de Cuyo and Comisión Nacional de Energía Atómica, Av. Bustillo 9500, 8400 S.C. de Bariloche, Argentina*

(Received 20 May 2016; revised manuscript received 17 August 2016; published 12 September 2016)

We present a fully relativistic formulation of the energy loss of a charged particle traversing a conductive monoatomic layer and apply it to the case of graphene in a transmission electron microscope (TEM). We use two models of conductivity appropriate for different frequency regimes: (a) THz (terahertz) frequency range and (b) optical range. In each range we distinguish two types of contributions to the electron energy loss: the energy deposited in graphene in the form of electronic excitations (Ohm losses), and the energy that is emitted in the form of radiation. We find strong relativistic effects in the electron energy loss spectra, which are manifested, e.g., in the increased heights of the principal π and $\sigma + \pi$ peaks that may be observed in TEM in the optical range. While the radiative energy losses are suppressed in the optical range in comparison to the Ohmic losses, we find that these two contributions are comparable in magnitude in the THz range, where the response of doped graphene is dominated by the Dirac plasmon polariton (DPP). In particular, relative contributions of the Ohmic and radiative energy losses are strongly affected by the damping of DPP. In the case of a clean graphene with low damping, the angular distribution of the radiated spectra at the sub-THz frequencies exhibit strong and possibly observable skewing towards graphene.

DOI: [10.1103/PhysRevB.94.125414](https://doi.org/10.1103/PhysRevB.94.125414)

I. INTRODUCTION

In the last twenty years, the field of nanoscience has vigorously developed, and its importance for technological applications has increased as miniaturization becomes more relevant in multiple areas, such as computing, sensors, biomedicine, etc. [1]. Currently, scientists continue examining materials with improved physicochemical properties that are dimensionally more suitable for specific applications.

In this context, the experimental discovery of two-dimensional graphene by Novoselov *et al.* [2] was an important contribution in the area of nanoscience, opening new frontiers in solid state physics due to its unique properties. As a one-atom-thick material, graphene attracts both academic and industrial interest. The two-dimensional (2D) character of graphene sheets improves many of the remarkable characteristics of carbon materials [3], such as thermal conductivity, mechanical and electronic properties [4–6]. These open new possibilities in the development of high speed and radio frequency logic devices, thermally and electrically conducting reinforced nanocomposites, electronic circuits, etc. [7–9]. Also, as a nanofiller, graphene may be preferred over other conventional fillers (Na-MMT, LDH, CNT, etc.) owing to its characteristics [8–10].

Graphene also shows remarkable optical properties, which make it stand out among other 2D materials for nanophotonic and optoelectronic applications [11]. Recent results show advances for its use in solar cells, light-emitting devices, touch

screens, photodetectors, and ultrafast lasers [12]. In particular, graphene plasmons (i.e., collective oscillations of its valence electrons) have been detected and are being analyzed as a useful tool for fast electronic manipulation of light, giving place to a vast range of fundamental studies and technological applications [13]. Particularly promising for applications in the frequency range from terahertz (THz) to the infrared (IR) is the so-called Dirac plasmon (or sheet plasmon), which arises from intraband excitations of the π electrons/holes in heavily doped graphene [13]. This collective mode is highly tunable by changing the chemical potential in graphene via external gates, whereas the corresponding plasmon polariton exhibits strong field confinement in the direction perpendicular to graphene with relatively long propagation distances along graphene [14].

As a fundamental technique to study the electronic and optical properties of nanostructures, electron energy loss spectroscopy (EELS) has been extensively used to characterize single- and multilayer graphene [15,16]. This technique is performed in transmission electron microscopes (TEM) with high-energy electron beams (~ 100 keV), for which relativistic effects could be important. The EELS-TEM configuration facilitates high-precision measurements of inelastic energy losses corresponding to the range of frequencies from visible to the ultraviolet (UV), which are dominated by the interband transitions of graphene's π and σ electrons [15,17,18]. Although nonretarded calculations have reproduced the experimental energy loss spectra for graphene quite successfully [15,19–21], a quantitative assessment of the importance of the relativistic correction to those spectra is needed for a broad range of the electron energy losses [15,22].

In recent years there has been a surge of interest in using electron beams to generate radiation from graphene in a range of frequencies from THz (terahertz) [23,24] to IR to x

*segui@cab.cnea.gov.ar

†Also at Consejo Nacional de Investigaciones Científicas y Técnicas de Argentina (CONICET).

rays [25] under a variety of the incident electron trajectories, including aloof scattering [23], cyclotron electron beam [24], and free electron beam [25]. It should be pointed out that the setting of a TEM experiment is also suitable for measurements of the cathodoluminescence (CL) light emission from the target material [22,26,27]. However, some aspects of the radiation processes induced by the incident particle in TEM remain unexplored, such as the transition radiation (TR) patterns in the presence of plasmon fields in graphene in a broad range of frequencies.

In this work, we evaluate both the relativistic corrections to the EELS and the TR spectra in the THz to UV frequency range, arising from a single layer of free graphene due to passage of a 100 keV electron under the normal incidence in TEM. This is achieved by using a relativistic formulation of the electromagnetic fields [28] and modeling the 2D conductivity of graphene within the well-known dielectric response formalism [29] with parameters that provide an adequate description of the dynamic response of graphene in a broad range of frequencies [19,30–32]. While this simple setting is relevant for the EELS-TEM experiments, it enables us to eliminate other sources of radiation, such as the TR from dielectric boundaries, Cherenkov radiation, braking radiation, and the possible CL from graphene. Taking advantage of such setting, we demonstrate the energy balance in the EELS by evaluating exact fractions of the electron energy losses that go into the Joule energy (or Ohmic heating) in graphene and the electromagnetic energy radiated in the far field region.

In the THz range, we use the well-known Drude model of the 2D conductivity in doped graphene, which shows that the spectra due to heating and radiation are comparable in magnitude in the THz range of frequencies and that the relative roles of those two mechanisms of energy loss are strongly influenced by the damping rate of the Dirac plasmon polariton (DPP) in graphene. Given that the dispersion of DPP is completely squeezed out of the light cone, it is surprising how the energy loss spectra are dominated by the radiated part as the frequency decreases in the sub-THz domain. While our prediction of the quite large relativistic effects in the EELS may be difficult to observe in a TEM in the THz-frequency range, the effects of damping may be readily observed in measurements of the angular distribution of the radiated spectra in that range of frequencies. On the other hand, in the visible to UV range we use the Drude-Lorentz model of graphene's conductivity [19,21] to show that the relativistic effect in the EELS mostly act to increase the height of the principal π and $\sigma + \pi$ peaks of graphene by some 10%. At the same time, the radiated energy spectra in that range of frequencies are heavily suppressed in magnitude with respect to the Ohmic heating of graphene, while displaying red-shifted peak structure of the EELS in graphene.

The present paper is organized as follows. In Sec. II, we start with a thorough description of the theory used. In particular, we present detailed expressions for the electromagnetic fields (Sec. II A), the energy loss formulas used to calculate the spectra (Sec. II B), and the models of conductivity applied in different frequency regimes (Sec. II C). Section III is devoted to showing and discussing the principal results obtained for monolayer graphene. Finally, our concluding remarks are

given in Sec. IV. Note that, unless otherwise explicitly stated, we use Gaussian units of electrodynamics [33].

II. THEORY

We consider a uniformly moving point charge that traverses a planar conducting layer with large area and zero thickness under normal incidence. This corresponds to the configuration of EELS for a one-atom thick sample such as single-layer graphene in a scanning transmission microscope (STEM). With the electron kinetic energy of the order of 100 keV, it is conceivable that dynamic polarization of the layer will exhibit strong retardation effects. Assuming that the layer is placed in vacuum and neglecting the change in momentum of the incident electron, we discard the Cherenkov radiation and braking radiation, as well as transition radiation arising from a boundary between two semi-infinite dielectrics [33,34]. Hence we focus our attention on the electromagnetic radiation coming from the charge currents induced in the conducting layer, which may also be called transition radiation (TR). In addition, we study the retardation effects in the energy loss spectra of the incident electron, especially in the presence of plasmon modes in the conducting layer. For simplicity, we assume that the layer is isotropic and homogeneous in 2D, so that its dielectric response may be described by a scalar conductivity $\sigma(k, \omega)$, which generally depends on both the 2D wave number k and frequency ω . In our applications to graphene, we shall use conductivity in the local approximation to explore two regimes: one that pertains to the THz plasmonic applications of doped graphene based on its Dirac (or sheet) plasmon mode, and the other that is concerned with probing the π and $\sigma + \pi$ spectral features of graphene by means of EELS in STEM, which occur at around 4 and 14 eV, respectively.

A. Self-consistent solution for the induced fields

We use the Hertz vector $\Pi(\mathbf{R}, t)$ [28] to describe the electric and magnetic fields generated by the external and induced currents in the system. It is convenient to perform the Fourier transform with respect to time via

$$\Pi(\mathbf{R}, \omega) = \int_{-\infty}^{\infty} dt e^{i\omega t} \Pi(\mathbf{R}, t), \quad (1)$$

where $\mathbf{R} = \{x, y, z\}$ is a point in a three-dimensional (3D) Cartesian coordinate system. Then, in an infinite, nonmagnetic medium described by a frequency dependent relative dielectric constant $\epsilon(\omega)$, the magnetic field and the electric field may be obtained from

$$\mathbf{H}(\mathbf{R}, \omega) = -i \frac{\omega}{c} \epsilon(\omega) \nabla \times \Pi(\mathbf{R}, \omega), \quad (2)$$

$$\mathbf{E}(\mathbf{R}, \omega) = \nabla(\nabla \cdot \Pi(\mathbf{R}, \omega)) + \frac{\omega^2}{c^2} \epsilon(\omega) \Pi(\mathbf{R}, \omega), \quad (3)$$

respectively, where c is the speed of light in vacuum. Assuming that the conducting layer is placed in the plane $z = 0$, it is also adequate to use Fourier transform with respect to the in-plane coordinates ($\mathbf{r} = \{x, y\} \rightarrow \mathbf{k} = \{k_x, k_y\}$), leaving explicit dependence on z . In the presence of a charge current with density $\mathbf{J}(\mathbf{k}, z, \omega)$ in vacuum (i.e., setting $\epsilon = 1$), the Hertz

vector is obtained by solving the equation [28]

$$\left(\frac{\partial^2}{\partial z^2} - k^2 + \frac{\omega^2}{c^2}\right) \mathbf{\Pi}(\mathbf{k}, z, \omega) = -\frac{4\pi i}{\omega} \mathbf{J}(\mathbf{k}, z, \omega), \quad (4)$$

where $k = \sqrt{k_x^2 + k_y^2}$. This equation may be solved for arbitrary current density \mathbf{J} as

$$\mathbf{\Pi}(\mathbf{k}, z, \omega) = \frac{i}{\omega} \int_{-\infty}^{\infty} dz' G(k, z - z', \omega) \mathbf{J}(\mathbf{k}, z', \omega), \quad (5)$$

where G is the retarded Green function (GF) [34] obtained in Appendix A:

$$G(k, z, \omega) = \begin{cases} \frac{2\pi i}{\kappa(k, \omega)} e^{i|z|\kappa(k, \omega)}, & |\omega| > ck \\ \frac{2\pi}{\alpha(k, \omega)} e^{-|z|\alpha(k, \omega)}, & |\omega| < ck \end{cases}, \quad (6)$$

with

$$\kappa(k, \omega) = \frac{\omega}{c} \sqrt{1 - \left(\frac{ck}{\omega}\right)^2}, \quad \text{for } |\omega| > ck, \quad (7)$$

$$\alpha(k, \omega) = \frac{|\omega|}{c} \sqrt{\left(\frac{ck}{\omega}\right)^2 - 1}, \quad \text{for } |\omega| < ck. \quad (8)$$

It is clear from Eq. (6) that κ defines the wave number of waves propagating in the far-field region as $|z| \rightarrow \infty$ when $|\omega| > ck$, whereas $\alpha > 0$ defines the evanescent solutions of Eq. (4) in the near-field region that are localized around the conducting layer when $|\omega| < ck$. In the following, we shall mostly show steps in our development of the theory that use the expression for the GF given in the first line of Eq. (6) for $|\omega| > ck$, but we note that a formal transition to the evanescent solution for $|\omega| < ck$ may be simply achieved in each step by the replacement $\kappa(k, \omega) \mapsto i\alpha(k, \omega)$.

We further assume that an external point charge Ze , where e is the charge of a proton, moves along the z axis with constant velocity $\mathbf{v} = \hat{\mathbf{z}}v$, where $\hat{\mathbf{z}}$ is a unit vector in the direction of that axis. Thus the Fourier transform of the current density due to the external charge with respect to \mathbf{r} and t is given by

$$\mathbf{J}_{\text{ext}}(\mathbf{k}, z, \omega) = Ze e^{iz\frac{\omega}{v}} \hat{\mathbf{z}}. \quad (9)$$

Upon substituting this expression for current in Eq. (5), the corresponding Hertz vector due to the external charge may be written in the form

$$\mathbf{\Pi}_{\text{ext}}(\mathbf{k}, z, \omega) = \frac{i}{\omega} A(k, \omega) \mathbf{J}_{\text{ext}}(\mathbf{k}, z, \omega), \quad (10)$$

where we have defined an auxiliary amplitude as

$$A(k, \omega) = \frac{4\pi}{\frac{\omega^2}{v^2} - \frac{\omega^2}{c^2} + k^2}. \quad (11)$$

As a consequence of the polarization of charge carriers in the conducting layer by the external charge, there will arise an in-plane current in that layer with the density $\mathbf{j}(\mathbf{k}, \omega)$. We allow that the scalar conductivity of the layer, $\sigma(k, \omega)$, may be a complex valued function and assume that it satisfies the condition $\sigma(k, -\omega) = \sigma^*(k, \omega)$, where $*$ indicates a complex conjugate, which guarantees causality of the layer's response. Then, the induced 2D current density in the conducting layer

may be expressed in terms of the tangential component of the total electric field, $\mathbf{E}_{\parallel}(\mathbf{k}, z, \omega)$, taken at the plane $z = 0$ as

$$\mathbf{j}(\mathbf{k}, \omega) = \sigma(k, \omega) \mathbf{E}_{\parallel}(\mathbf{k}, 0, \omega). \quad (12)$$

Taking into account that the conducting layer has zero thickness, the corresponding induced 3D current may be written in terms of Dirac's delta function as

$$\mathbf{J}_{\text{ind}}(\mathbf{k}, z, \omega) = \delta(z) \mathbf{j}(\mathbf{k}, \omega), \quad (13)$$

which when inserted into Eq. (5) gives an expression for the corresponding Hertz vector as

$$\mathbf{\Pi}_{\text{ind}}(\mathbf{k}, z, \omega) = \frac{i}{\omega} G(k, z, \omega) \sigma(k, \omega) \mathbf{E}_{\parallel}(\mathbf{k}, 0, \omega). \quad (14)$$

Now, the total Hertz vector is given by the sum of the external and induced fields, $\mathbf{\Pi} = \mathbf{\Pi}_{\text{ext}} + \mathbf{\Pi}_{\text{ind}}$; on the other hand, writing it as

$$\mathbf{\Pi}(\mathbf{k}, z, \omega) = \mathbf{\Pi}_{\parallel}(\mathbf{k}, z, \omega) + \hat{\mathbf{z}} \Pi_z(\mathbf{k}, z, \omega), \quad (15)$$

it is clear that its components in the directions parallel to the conducting layer, $\mathbf{\Pi}_{\parallel}(\mathbf{k}, z, \omega) \equiv \mathbf{\Pi}_{\text{ind}}(\mathbf{k}, z, \omega)$, are only determined by the induced current via Eqs. (12) and (14), whereas its component along the z axis, $\Pi_z(\mathbf{k}, z, \omega) \equiv \hat{\mathbf{z}} \cdot \mathbf{\Pi}_{\text{ext}}(\mathbf{k}, z, \omega)$, is only determined by the external charge via Eqs. (9) and (10).

Using Eq. (3) with $\epsilon = 1$, we express the total electric field \mathbf{E} in terms of $\mathbf{\Pi}$ as

$$\begin{aligned} \mathbf{E}(\mathbf{k}, z, \omega) = & \frac{\omega^2}{c^2} [\mathbf{\Pi}_{\parallel}(\mathbf{k}, z, \omega) + \hat{\mathbf{z}} \Pi_z(\mathbf{k}, z, \omega)] + \left(i\mathbf{k} + \hat{\mathbf{z}} \frac{\partial}{\partial z} \right) \\ & \times \left[i\mathbf{k} \cdot \mathbf{\Pi}_{\parallel}(\mathbf{k}, z, \omega) + \frac{\partial}{\partial z} \Pi_z(\mathbf{k}, z, \omega) \right], \end{aligned} \quad (16)$$

wherefrom the tangential component of the total electric field taken at the plane $z = 0$ is obtained as

$$\begin{aligned} \mathbf{E}_{\parallel}(\mathbf{k}, 0, \omega) = & \left(\frac{\omega^2}{c^2} - \mathbf{k} \cdot \mathbf{k} \right) \mathbf{\Pi}_{\parallel}(\mathbf{k}, 0, \omega) \\ & + i\mathbf{k} \frac{\partial}{\partial z} \Pi_z(\mathbf{k}, z, \omega) \Big|_{z=0}. \end{aligned} \quad (17)$$

Using Eqs. (6) and (14) at $z = 0$, we write

$$\mathbf{\Pi}_{\parallel}(\mathbf{k}, 0, \omega) \equiv \mathbf{\Pi}_{\text{ind}}(\mathbf{k}, 0, \omega) = -\frac{2\pi\sigma}{\omega\kappa} \mathbf{E}_{\parallel}(\mathbf{k}, 0, \omega), \quad (18)$$

while using Eqs. (9) and (10), we have

$$\begin{aligned} \frac{\partial}{\partial z} \Pi_z(\mathbf{k}, z, \omega) \Big|_{z=0} & \equiv \frac{\partial}{\partial z} [\hat{\mathbf{z}} \cdot \mathbf{\Pi}_{\text{ext}}(\mathbf{k}, z, \omega)] \Big|_{z=0} \\ & = -\frac{Ze}{v} A(k, \omega). \end{aligned} \quad (19)$$

Substituting the final expressions from Eqs. (18) and (19) into the right hand side of Eq. (17), we find a self-consistent solution for the longitudinal component of the total tangential electric

field in the plane of the conducting layer as

$$\mathbf{E}_{\parallel}(\mathbf{k}, 0, \omega) = -i\mathbf{k} \frac{Ze}{v} \frac{A(k, \omega)}{1 + \frac{2\pi}{\omega} \kappa \sigma}. \quad (20)$$

Inserting the result from Eq. (20) into Eq. (14) and using Eq. (6), we finally obtain the induced Hertz vector as [in the following we simplify the notation by writing $A(k, \omega) \rightarrow A$]

$$\mathbf{\Pi}_{\text{ind}}(\mathbf{k}, z, \omega) = i\mathbf{k} \frac{Ze}{v} \frac{A}{\omega \kappa} \frac{2\pi \sigma}{(1 + \frac{2\pi}{\omega} \kappa \sigma)} e^{i|z|\kappa}. \quad (21)$$

We can further obtain an expression for the induced electric field from Eq. (16) by setting $\Pi_z(\mathbf{k}, z, \omega) = 0$ and using the expression from Eq. (21) in place of $\mathbf{\Pi}_{\parallel}(\mathbf{k}, z, \omega)$ as follows:

$$\mathbf{E}_{\text{ind}}(\mathbf{k}, z, \omega) = i[\mathbf{k}\kappa - \hat{\mathbf{z}}k^2 \text{sgn}(z)] \frac{Ze}{v} \frac{A}{\omega} \frac{2\pi \sigma}{1 + \frac{2\pi}{\omega} \kappa \sigma} e^{i|z|\kappa}, \quad (22)$$

where sgn is the standard signum function.

From Eq. (21) and the definition for the magnetic field \mathbf{H} in terms of $\mathbf{\Pi}$, Eq. (2) with $\epsilon = 1$, we obtain the induced magnetic field as

$$\begin{aligned} \mathbf{H}_{\text{ind}}(\mathbf{k}, z, \omega) &= -i \frac{\omega}{c} \left(i\mathbf{k} + \hat{\mathbf{z}} \frac{\partial}{\partial z} \right) \times \mathbf{\Pi}_{\text{ind}}(\mathbf{k}, z, \omega) \\ &= i \frac{\omega}{c} (\hat{\mathbf{z}} \times \mathbf{k}) \frac{Ze}{v} \frac{A}{\omega} \frac{2\pi \sigma}{1 + \frac{2\pi}{\omega} \kappa \sigma} e^{i|z|\kappa} \text{sgn}(z). \end{aligned} \quad (23)$$

Notice that the expressions in Eqs. (22) and (23) are strictly valid inside the light cone, $|\omega| > ck$, that is, in the far-field region with κ given in Eq. (7). In order to convert those expressions to evanescent solutions in the near-field region where $|\omega| < ck$, one has to replace $\kappa \mapsto i\alpha$ so that the relevant factors in Eqs. (22) and (23) transform according to

$$\frac{e^{i|z|\kappa}}{1 + \frac{2\pi}{\omega} \kappa \sigma} \mapsto \frac{e^{-|z|\alpha}}{1 + i \frac{2\pi}{\omega} \alpha \sigma}, \quad (24)$$

with $\alpha > 0$ given in Eq. (8).

In the following sections, we shall rely on a property that implies that $\mathbf{E}_{\text{ind}}(-\mathbf{k}, z, -\omega) = \mathbf{E}_{\text{ind}}^*(\mathbf{k}, z, \omega)$ and $\mathbf{H}_{\text{ind}}(-\mathbf{k}, z, -\omega) = \mathbf{H}_{\text{ind}}^*(\mathbf{k}, z, \omega)$, where $*$ indicates complex conjugation of each vector component in the Fourier transforms of the real valued fields $\mathbf{E}_{\text{ind}}(\mathbf{r}, z, t)$ and $\mathbf{H}_{\text{ind}}(\mathbf{r}, z, t)$. This property is ensured in the expressions in Eqs. (22) and (23) by considering the parity of A , σ , κ , and α as functions of ω .

We conclude this subsection by making a comment that the final expressions for the induced fields in Eqs. (22) and (23) guarantee that the corresponding total fields, $\mathbf{E}(\mathbf{k}, z, \omega)$ and $\mathbf{H}(\mathbf{k}, z, \omega)$, satisfy the usual jump boundary conditions at $z = 0$. [33] Namely, using Eq. (23) one can show that

$$\hat{\mathbf{z}} \times [\mathbf{H}(\mathbf{k}, 0^+, \omega) - \mathbf{H}(\mathbf{k}, 0^-, \omega)] = \frac{4\pi}{c} \mathbf{j}(\mathbf{k}, \omega), \quad (25)$$

where we have used Eqs. (12) and (20) to reconstruct an expression for the 2D current density $\mathbf{j}(\mathbf{k}, \omega)$ in the conducting layer. On the other hand, using Eq. (22), we find

$$\hat{\mathbf{z}} \cdot [\mathbf{E}(\mathbf{k}, 0^+, \omega) - \mathbf{E}(\mathbf{k}, 0^-, \omega)] = 4\pi \rho(\mathbf{k}, \omega), \quad (26)$$

where we have used a 2D continuity equation to express the surface density of charge induced in the conducting layer as $\rho = \mathbf{k} \cdot \mathbf{j}/\omega$.

B. Energy loss of the external charge

The energy loss spectrum recorded in an EELS experiment can be obtained from the total work done by the induced electric field on the external charge, given by

$$\begin{aligned} W_{\text{ext}} &= \int_{-\infty}^{\infty} dt \iiint d^3\mathbf{R} \mathbf{J}_{\text{ext}}(\mathbf{R}, t) \cdot \mathbf{E}_{\text{ind}}(\mathbf{R}, t) \\ &= -i \frac{(Ze)^2}{v} \iint \frac{d^2\mathbf{k}}{(2\pi)^2} k^2 \int_{-\infty}^{\infty} \frac{d\omega}{\omega} \frac{A \sigma}{1 + \frac{2\pi}{\omega} \kappa \sigma} \\ &\quad \times \int_{-\infty}^{\infty} dz e^{-iz \frac{\omega}{v} + i|z|\kappa} \text{sgn}(z), \end{aligned} \quad (27)$$

where we have used Eq. (9) and the z component of the induced field in Eq. (22). The integral over z in the last line of Eq. (27) is well-defined for $|\omega| < ck$ when $\kappa \mapsto i\alpha$ with $\alpha > 0$. In the case when $|\omega| > ck$ and hence κ is real valued, one must insert a convergence factor $e^{-\eta|z|}$ in the z integral according to the change $\kappa \mapsto \kappa + i\eta$ and eventually take the limit $\eta \rightarrow 0^+$. This formal trick may be justified by assuming a slightly lossy medium in the far-field regions with $\Im[\epsilon(\omega)] \rightarrow 0^+$. In either case, the result of integration over z in the last line of Eq. (27) is $-i\omega A/(2\pi v)$ for arbitrary ω , giving

$$\begin{aligned} W_{\text{ext}} &= -\frac{(Ze)^2}{\pi v^2} \iint \frac{d^2\mathbf{k}}{(2\pi)^2} k^2 \int_0^{\infty} d\omega A^2 \Re \\ &\quad \times \left[\frac{\sigma(k, \omega)}{1 + \frac{2\pi}{\omega} \kappa(k, \omega) \sigma(k, \omega)} \right]. \end{aligned} \quad (28)$$

Here, we have reduced the integration over frequencies to positive values by using the parity properties of the functions $\sigma(k, \omega)$, $A(k, \omega)$, $\kappa(k, \omega)$, and $\alpha(k, \omega)$.

Note that the integrand in Eq. (28) is related to the probability density that the external charge will loose an energy $\hbar\omega$ and suffer a change in the momentum $\hbar\mathbf{k}$ perpendicular to its trajectory. To analyze its structure in some detail, we decompose the integral over ω in Eq. (28) over the near-field and far-field regions, respectively,

$$\begin{aligned} &\int_0^{\infty} d\omega A^2 \Re \left[\frac{\sigma}{1 + \frac{2\pi}{\omega} \kappa \sigma} \right] \\ &= \int_0^{ck} d\omega A^2 \frac{\Re[\sigma]}{|1 + i \frac{2\pi}{\omega} \alpha \sigma|^2} \\ &\quad + \int_{ck}^{\infty} d\omega A^2 \frac{\Re[\sigma] + \frac{2\pi}{\omega} \kappa |\sigma|^2}{|1 + \frac{2\pi}{\omega} \kappa \sigma|^2}. \end{aligned} \quad (29)$$

Since all terms in this expression are positive, one sees from Eq. (28) that generally $W_{\text{ext}} < 0$, so it may be written in the form

$$W_{\text{ext}} = - \iint d^2\mathbf{k} \int_0^{\infty} d\omega \omega F(\mathbf{k}, \omega), \quad (30)$$

which defines the total probability density $F(\mathbf{k}, \omega) > 0$.

The total energy change involved in the process is given by $W = W_{\text{ext}} + W_{\text{ohm}} + W_{\text{rad}}$, where W_{ext} is given by Eq. (27), W_{ohm} is the Joule energy that describes the Ohmic heating of the conducting layer, and W_{rad} is the total energy radiated by the electromagnetic fields at frequencies $\omega > ck$ in the far field

regions above and below the conducting layer. In Appendix B, we show that when the two terms with $\Re[\sigma]$ in Eq. (29) are used in Eq. (28), one obtains exactly $-W_{\text{ohm}}$. Also, we show that when the remaining term in Eq. (29) with $|\sigma|^2$ is used in Eq. (28), one obtains exactly $-W_{\text{rad}}$. Hence the balance of

energy in the system may be expressed as

$$W_{\text{ext}} + W_{\text{ohm}} + W_{\text{rad}} = 0 \quad (31)$$

with

$$W_{\text{ohm}} = \frac{(Ze)^2}{\pi v^2} \iint \frac{d^2 \mathbf{k}}{(2\pi)^2} \left\{ \int_0^{ck} d\omega \frac{(kA)^2 \Re[\sigma(k, \omega)]}{|1 + i \frac{2\pi}{c} \sigma(k, \omega) \sqrt{(\frac{ck}{\omega})^2 - 1}|^2} + \int_{ck}^{\infty} d\omega \frac{(kA)^2 \Re[\sigma(k, \omega)]}{|1 + \frac{2\pi}{c} \sigma(k, \omega) \sqrt{1 - (\frac{ck}{\omega})^2}|^2} \right\} \quad (32)$$

and

$$W_{\text{rad}} = \frac{2(Ze)^2}{c v^2} \iint \frac{d^2 \mathbf{k}}{(2\pi)^2} \int_{ck}^{\infty} d\omega (kA)^2 \sqrt{1 - \left(\frac{ck}{\omega}\right)^2} \left| \frac{\sigma(k, \omega)}{1 + \frac{2\pi}{c} \sigma(k, \omega) \sqrt{1 - \left(\frac{ck}{\omega}\right)^2}} \right|^2. \quad (33)$$

Accordingly, the total probability density for the energy loss and momentum transfer of the external charge, defined via Eq. (30), may be decomposed into two contributions, $F = F_{\text{ohm}} + F_{\text{rad}}$, corresponding to the Joule energy spent on Ohmic heating of the conducting layer,

$$F_{\text{ohm}}(k, \omega) = \frac{4(Ze)^2}{\pi \beta^2 \omega} \frac{(ck)^2 \Re[\sigma]}{[\omega^2 (\frac{1}{\beta^2} - 1) + (ck)^2]^2} \begin{cases} \frac{1}{|1 + \frac{2\pi}{c} \sigma \sqrt{1 - (\frac{ck}{\omega})^2}|^2}, & \omega > ck, \\ \frac{1}{|1 + i \frac{2\pi}{c} \sigma \sqrt{(\frac{ck}{\omega})^2 - 1}|^2}, & \omega < ck, \end{cases} \quad (34)$$

and the total radiated energy for $\omega > ck$ given by

$$F_{\text{rad}}(k, \omega) = 8 \frac{(Ze)^2}{\beta^2 \omega} \frac{ck^2 \sqrt{1 - (\frac{ck}{\omega})^2}}{[\omega^2 (\frac{1}{\beta^2} - 1) + (ck)^2]^2} \left| \frac{\sigma}{1 + \frac{2\pi}{c} \sigma \sqrt{1 - (\frac{ck}{\omega})^2}} \right|^2, \quad (35)$$

where $\beta = v/c$.

In EELS, one is often interested in the spectra integrated over the in-plane momentum transfer up to some critical value $k_s = \vartheta k_0$, which is defined by the effective scattering semi-angle of electron beam ϑ and the incident electron momentum $\hbar k_0$. The angle ϑ is defined by the beam convergence angle and the aperture collection angle [21]. Then, the corresponding marginal probability density for energy loss $\hbar\omega$ is obtained from Eq. (30) as

$$P(\omega) = \frac{1}{\hbar^2} \iint_{\|\mathbf{k}\| < k_s} d^2 \mathbf{k} F(k, \omega) = \frac{2\pi}{\hbar^2} \int_0^{k_s} dk k F(k, \omega). \quad (36)$$

We note that ϑ is typically on the order of some 10 mrad in EELS, but in practice the range of integration in Eq. (36) may be often extended to $k_s \rightarrow \infty$ [21]. As with the joint probability density $F(k, \omega)$, one may also decompose the total probability of energy loss into two contributions, $P = P_{\text{ohm}} + P_{\text{rad}}$, corresponding to the Joule energy and the radiated energy, respectively.

We finally note that, in the nonretarded limit, one lets $c \rightarrow \infty$, so that $F_{\text{rad}} \rightarrow 0$ in Eq. (35) and only the second line in the definition of F_{ohm} in Eq. (34) survives giving $F_{\text{ohm}} \rightarrow F_{\text{nonret}}$, where

$$F_{\text{nonret}}(k, \omega) = \frac{2}{\pi^2} (Zev)^2 \frac{k}{(\omega^2 + k^2 v^2)^2} \Im \left[\frac{-1}{\epsilon_{2D}(k, \omega)} \right]. \quad (37)$$

This expression for the probability density of energy loss and momentum transfer in the nonretarded limit was derived in previous works [19,21]. We have introduced in Eq. (37) the loss function of the conducting layer, $\Im[-1/\epsilon_{2D}]$, which is expressed in terms of its 2D dielectric function defined by $\epsilon_{2D}(k, \omega) = 1 + i2\pi \frac{k}{\omega} \sigma(k, \omega)$.

It is of further interest to find the joint spectral density and the angular distribution of the TR given in Eq. (33). For radiation emitted in both the upper and lower half-spaces at a frequency ω in a direction with the angle θ with respect to $\hat{\mathbf{z}}$ and with polar angle φ , one can write $\mathbf{k} = \{k_x, k_y\} = \frac{\omega}{c} \sin \theta \{\cos \varphi, \sin \varphi\}$, and hence $d^2 \mathbf{k} = dk_x dk_y = \frac{\omega^2}{c^2} \sin \theta |\cos \theta| d\theta d\varphi$ in Eq. (33). Thus one obtains from Eq. (33)

$$W_{\text{rad}} = \iint d^2 \hat{\Omega} \int_0^{\infty} d\omega S(\theta, \omega), \quad (38)$$

where $S(\theta, \omega) \equiv \frac{\partial^3 W_{\text{rad}}}{\partial^2 \hat{\Omega} \partial \omega}$ is the total spectral density of radiation and $d^2 \hat{\Omega} = \sin \theta d\theta d\varphi$ is the infinitesimal solid angle for $0 \leq \theta \leq \pi$ and $0 < \varphi < 2\pi$ [35]. The function $S(\theta, \omega)$ is obtained by substituting $k = \frac{\omega}{c} \sin \theta$ and $\kappa = \frac{\omega}{c} |\cos \theta|$ in the integrand of Eq. (33). Noticing that the amplitude in Eq. (11) may be then written as

$$A = 4\pi \frac{c^2}{\omega^2} \frac{\beta^2}{1 - \beta^2 \cos^2 \theta}, \quad (39)$$

one obtains

$$S(\theta, \omega) = Z^2 \frac{e^2}{c} \left[\frac{\beta \sin(2\theta)}{1 - \beta^2 \cos^2 \theta} \right]^2 \times \left| \frac{\sigma\left(\frac{\omega}{c} \sin \theta, \omega\right)}{c + 2\pi |\cos \theta| \sigma\left(\frac{\omega}{c} \sin \theta, \omega\right)} \right|^2. \quad (40)$$

We note that an alternate derivation of this result may be obtained from an asymptotic analysis of spherical waves in the far region due to Weyl [36,37], as outlined at the end of Appendix B.

C. Models of 2D conductivity

The conductivity of a 2D layer may be expressed in terms of its polarizability function, or the density-density response function of noninteracting electrons in that layer, χ_0 , as

$$\sigma(k, \omega) \equiv -ie^2 \omega \frac{\chi_0(k, \omega)}{k^2}. \quad (41)$$

The formalism developed in the preceding subsections can be directly applied to any 2D material described by a nonlocal scalar conductivity [11], and it may be readily generalized to anisotropic 2D materials [38]. In order to explore the leading effects due to retardation in the EELS and the properties of TR in the presence of plasmon mode(s) in a 2D material, we shall further focus our attention on the optical limit where conductivity of the layer only depends on frequency, $\sigma(\omega)$. While this regime is of primary interest in photonic applications of layered structures, it is also expected that the retardation effects in EELS will be most pronounced in the optical limit. In that limit, several empirical models for $\sigma(\omega)$ are available in various frequency ranges for different 2D materials [38] including graphene [19], whereas *ab initio* methods may also be utilized to obtain $\sigma(\omega)$ by taking the limit $k \rightarrow 0$ in Eq. (41) [20,21,39].

For a quasifree, 2D electron gas (2DEG) at low frequencies, one may use the Drude model for conductivity [40,41]

$$\sigma_D(\omega) = i \frac{v_B}{\pi} \frac{\omega_F}{\omega + i\gamma}, \quad (42)$$

where $v_B = e^2/\hbar \approx c/137$ is the Bohr velocity, $\omega_F = \varepsilon_F/\hbar$ is the frequency related to the Fermi energy ε_F , and γ is the damping rate. For a 2DEG with single parabolic energy band, one has $\omega_F = \pi \hbar n_0/m_*$, where n_0 is the equilibrium electron areal density and m_* the effective electron mass [40], whereas for the Dirac electrons in a heavily doped graphene one has $\omega_F = v_F k_F$, where $v_F \approx c/300$ is the Fermi speed in graphene and $k_F = \sqrt{\pi|n|}$ its Fermi wave number [41].

In the case of doped graphene, the Drude conductivity model in Eq. (42) describes the collective, *intraband* excitation mode of graphene's π electron bands considered in the Dirac cone approximation. This mode is commonly described as the Dirac (or sheet) plasmon, which has an appealing property of tunability of its dispersion relation by controlling the doping density of charge carriers in graphene, n , using external means [42]. It turns out that the validity of Eq. (42) is limited by the relations $k v_F \ll \omega \ll \omega_F$, so that for typical doping densities of $|n| \lesssim 10^{13} \text{ cm}^{-2}$, the corresponding Fermi energy of $\varepsilon_F = \hbar v_F k_F \lesssim 0.4 \text{ eV}$ guarantees that this model is suitable for

studying the Dirac plasmon for applications in the THz to mid-infrared (MIR) range of frequencies [43]. Besides its tunability, the Dirac plasmon in graphene is expected to be relatively long lived: one may estimate its damping rate to be $\hbar\gamma \sim 1 \text{ meV}$ by equating the static limit of the Drude conductivity, $\sigma_D(0) = v_B \omega_F/(\pi\gamma)$, with the dc conductivity, $\sigma_{dc} = e|n|\mu$. This gives an estimate for the damping as $\gamma = v_B v_F/(e\mu k_F)$, where μ is the mobility of charge carriers, which may take rather large values, well in excess of $10^5 \text{ cm}^2/(\text{Vs})$ in clean graphene [42].

In order to extend the applicability of the Drude model in Eq. (42) for doped graphene in the optical limit to frequencies beyond $2\omega_F$, it is necessary to use the sum of conductivities, $\sigma_D + \sigma_{\text{Dirac}}$, where contribution from the *interband* electron transitions in the Dirac cone approximation is given at zero temperature by

$$\sigma_{\text{Dirac}}(\omega) = \frac{v_B}{4} \left[\Theta(\omega - 2\omega_F) + \frac{i}{\pi} \ln \left| \frac{\omega - 2\omega_F}{\omega + 2\omega_F} \right| \right], \quad (43)$$

with Θ being the Heaviside unit step function. The above model is valid for frequencies up to about $\hbar\omega \sim 2 \text{ eV}$. In the case of neutral, or intrinsic graphene, when $n = 0$ and hence $\omega_F = 0$, one has $\sigma_D = 0$, so the only contribution to the low-frequency conductivity of undoped graphene follows from Eq. (43) to be $\sigma_{\text{Dirac}} = v_B/4$ [43].

In the range of high frequencies, $\hbar\omega \gtrsim 2 \text{ eV}$, when the optical response of graphene is dominated by the $\pi \rightarrow \pi^*$ and $\sigma \rightarrow \sigma^*$ interband transitions at high-symmetry points of the Brillouin zone [44,45], one may use a Drude-Lorentz model of conductivity in the optical limit, given by [19,21]

$$\sigma_{DL}(\omega) = ie^2 \omega \left[\frac{n_\pi^0/m_\pi^*}{\omega(\omega + i\gamma_\pi) - \omega_{\pi r}^2} + \frac{n_\sigma^0/m_\sigma^*}{\omega(\omega + i\gamma_\sigma) - \omega_{\sigma r}^2} \right]. \quad (44)$$

The above model may be derived from a 2D, two-fluid hydrodynamic model of graphene's π and σ electron bands, where n_v^0 , m_v^* , ω_{vr} , and γ_v are the equilibrium surface number density of electrons, effective electron mass, restoring frequency, and the damping rate in the v th fluid (where $v = \pi, \sigma$), respectively. By using the model in Eq. (44) with the following parameters: $n_\pi^0 = 38 \text{ nm}^{-2}$, $n_\sigma^0 = 114 \text{ nm}^{-2}$, $\omega_{\pi r} = 4.08 \text{ eV}$, $\omega_{\sigma r} = 13.6 \text{ eV}$, $\gamma_\pi = 1.958 \text{ eV}$, $\gamma_\sigma = 2.176 \text{ eV}$, along with $m_\sigma^* = m_\pi^* = m_0$ (free electron mass), several sets of experimental data for EELS on single layered graphene for $\hbar\omega \gtrsim 2 \text{ eV}$ could be reproduced at the qualitative and semi-quantitative levels [15,19,21].

We finally note that it may be possible to extend the domains of applicability for the above models for neutral graphene by combining the expressions in Eqs. (43) and (44) [46]. Alternatively, instead of analytical models one may use the results of *ab initio* calculations, which were recently obtained by Novko *et al.* [39] for the conductivity of neutral graphene in the optical limit.

III. RESULTS AND DISCUSSION

In this section, we present calculations corresponding to the energy loss of electrons impinging on 2D graphene, using the conductivity models described in the previous section for different frequency regimes. It is interesting to note that, when

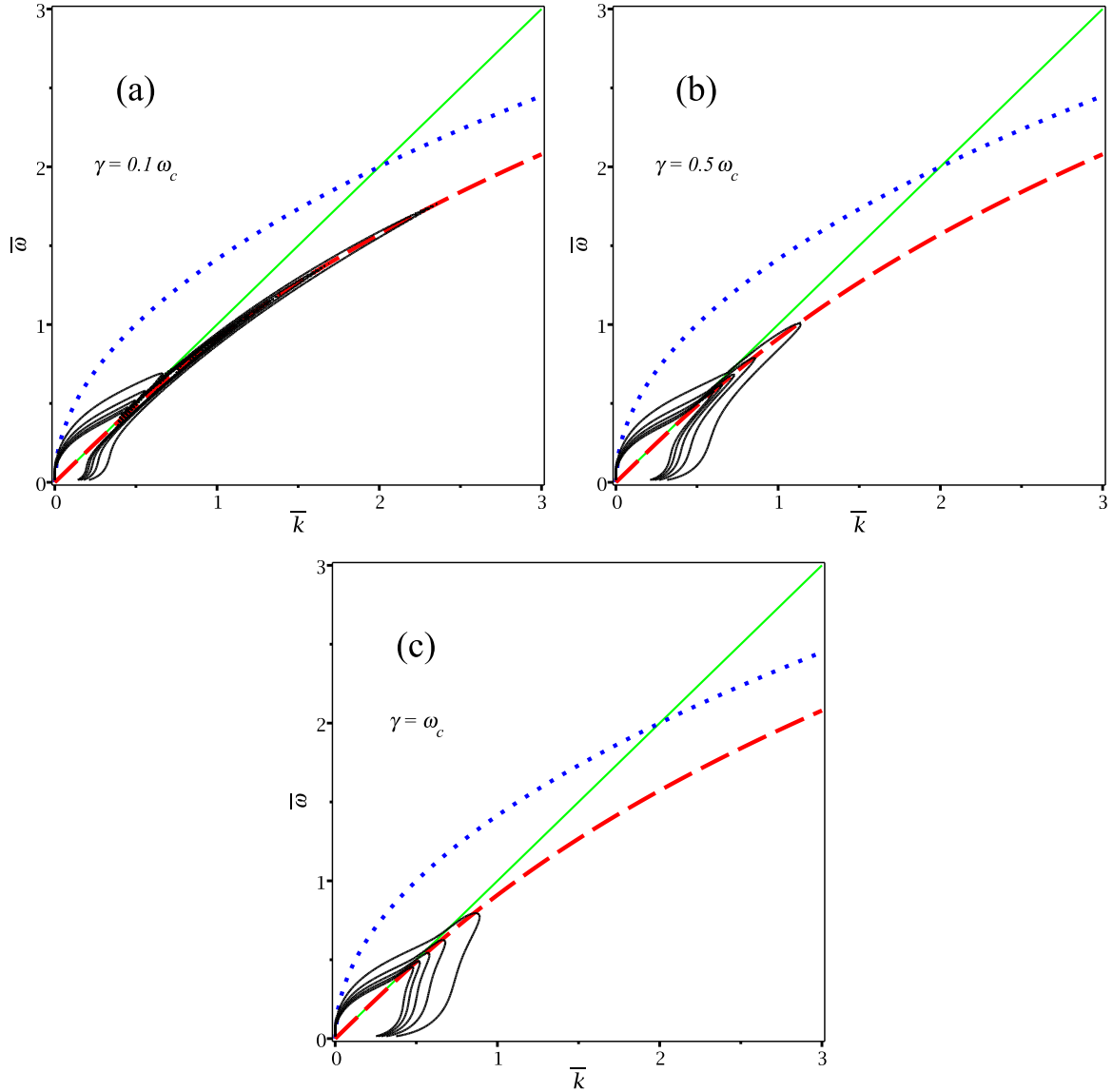


FIG. 1. Total probability density F , obtained from Eqs. (34) and (35), for energy loss $\hbar\omega$ and momentum transfer $\hbar k$ of a 100 keV electron passing through a layer of doped graphene described by the Drude conductivity, Eq. (42), with damping rates (a) $\gamma = 0.1\omega_c$, (b) $0.5\omega_c$, and (c) ω_c . Level curves (thin solid black lines) are shown for the reduced probability density $\bar{F} = F/F_c$ in the range $0 < \bar{F} \leq 1$ with the steps of 0.2 versus reduced frequency $\bar{\omega} = \omega/\omega_c$ and the reduced wave number $\bar{k} = k/k_c$, where $F_c = 4e^2/(\pi\omega_c^2 k_c)$, $\omega_c = ck_c$, and $k_c = k_F v_B v_F / c^2$. Also shown are the dispersion of light, $\bar{\omega} = \bar{k}$ (solid green line), the dispersion of the Dirac plasmon in nonretarded limit, $\bar{\omega} = \sqrt{2}\bar{k}$ (dotted blue line), and the dispersion of the Dirac plasmon polariton, $\bar{\omega} = \sqrt{2(-1 + \sqrt{1 + \bar{k}^2})}$ (dashed red line).

one uses a local model of conductivity, $\sigma(\omega)$, in $F_{\text{ohm}}(k, \omega)$ and $F_{\text{rad}}(k, \omega)$, Eqs. (34) and (35), it is possible to compute the k integral in Eq. (36), and hence obtain analytical expressions for the marginal probability density $P(\omega)$ for both the Joule and radiative energy losses, respectively.

A. Terahertz frequencies

Let us first examine the low-frequency regime dominated by the Dirac plasmon mode, using the Drude conductivity expression (42). It is instructive to show the effects of retardation on the dispersion of Dirac plasmon in graphene by considering possible resonances in Eq. (29) with damping set to $\gamma = 0$. While the denominator in the second term

of that expression has no real zeros for $\omega > ck$, we find a resonant plasmon-polariton mode by solving the equation $1 + 2\pi i \alpha \sigma_D / \omega = 0$ for $0 < \omega < ck$. This gives a dispersion relation for Dirac plasmon-polariton (DPP) defined by

$$\omega^2 = 2\omega_F^2 \left[-\left(\frac{v_B}{c}\right)^2 + \sqrt{\left(\frac{v_B}{c}\right)^4 + \left(\frac{v_B}{v_F} \frac{k}{k_F}\right)^2} \right]. \quad (45)$$

One can show that for very long wavelengths, $k \ll k_F v_B v_F / c^2$, the dispersion relation in Eq. (45) approaches the light line, $\omega = ck$, whereas when an opposite inequality holds, then the dispersion approaches the typical relation of the Dirac plasmon in the nonretarded limit at long wavelengths,

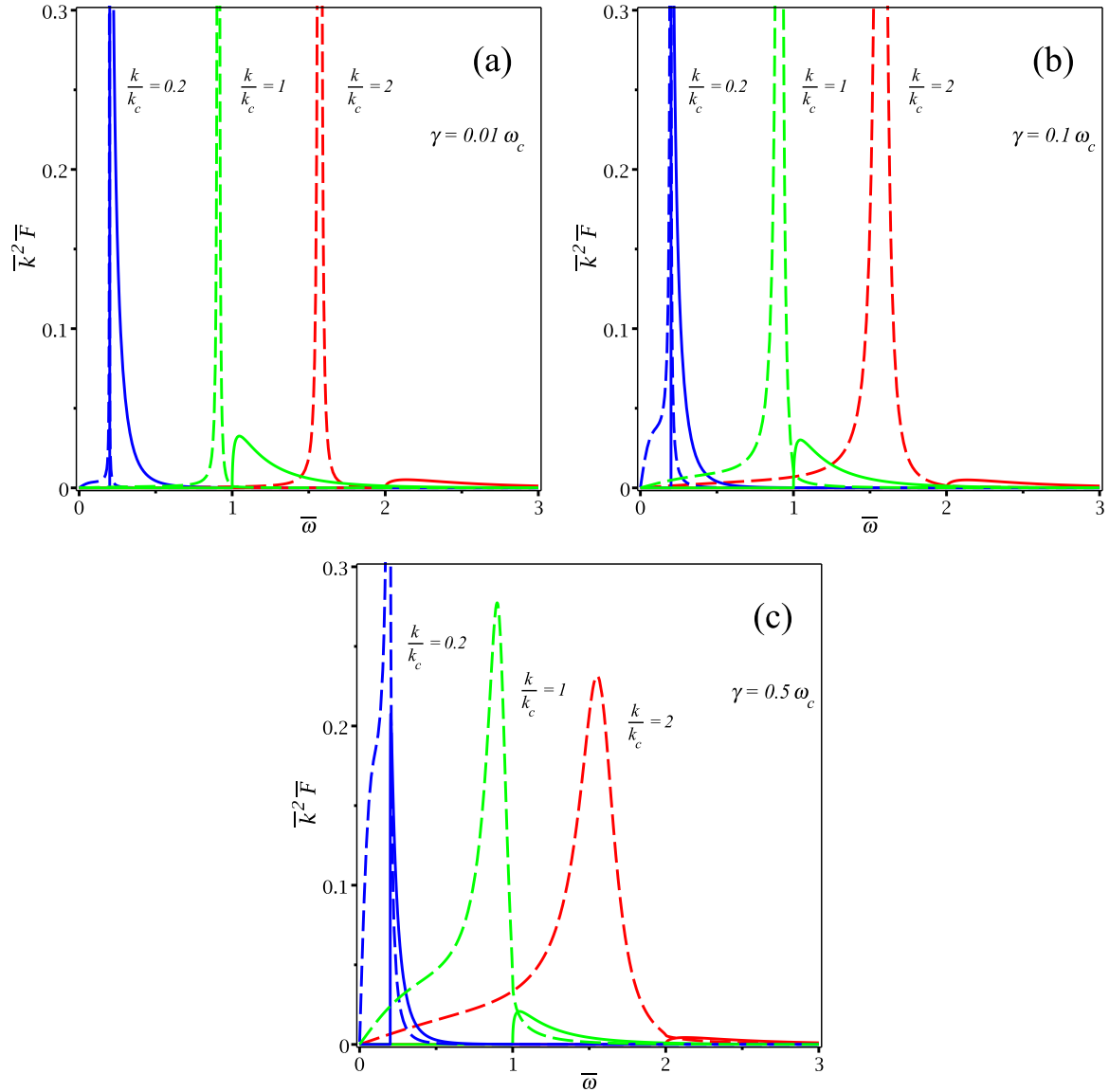


FIG. 2. Contributions to the probability density F for energy loss $\hbar\omega$ and momentum transfer $\hbar k$ of a 100 keV electron passing through a layer of doped graphene described by the Drude conductivity, Eq. (42), with damping rates (a) $\gamma = 0.01\omega_c$, (b) $0.1\omega_c$, and (c) $0.5\omega_c$. Vertical cross sections are shown for the reduced probability density $\bar{F} = F/F_c$ multiplied by the square of the reduced wave number $\bar{k} = k/k_c$ for $\bar{k} = 0.2$ (blue lines), 1 (green lines), and 2 (red lines) as functions of the reduced frequency $\bar{\omega} = \omega/\omega_c$, where $F_c = 4e^2/(\pi\omega_c^2 k_c)$, $\omega_c = ck_c$, and $k_c = k_F v_B v_F / c^2$. Solid lines show the contributions to $\bar{k}^2 \bar{F}$ from the radiated energy given in Eq. (35), whereas the dashed lines show the contributions from the Joule energy given in Eq. (34).

$\omega = \sqrt{2v_B v_F k_F k}$. Therefore a transition between the two limits occurs for wave numbers k in the neighborhood of the characteristic wave number $k_c = v_B v_F k_F / c^2$, which attains values $k_c \lesssim 1.36 \times 10^{-5} \text{ nm}^{-1}$ for doping densities $|n| \lesssim 10^{13} \text{ cm}^{-2}$. If one defines the corresponding characteristic angular frequency as $\omega_c = ck_c = v_B v_F k_F / c$, so that $\hbar\omega_c \lesssim 2.69 \text{ meV}$ or $\nu_c = \omega_c/(2\pi) \lesssim 0.65 \text{ THz}$, then the dispersion relation in Eq. (45) may be written in a dimensionless form

as $\bar{\omega} = \sqrt{2(-1 + \sqrt{1 + \bar{k}^2})}$, where $\bar{k} = k/k_c$ and $\bar{\omega} = \omega/\omega_c$ are the reduced wave number and frequency, respectively. This relation is shown in all three panels of Fig. 1 along with the dispersion of light, $\bar{\omega} = \bar{k}$, and the dispersion of the Dirac plasmon in nonretarded limit, $\bar{\omega} = \sqrt{2\bar{k}}$, in the

reduced units. Clearly, the dispersion of the DPP given via Eq. (45) is completely “squeezed out” of the light line in the limit $\gamma \rightarrow 0$. In practice, however, a well-defined DPP may only exist if $\gamma \ll \omega_c$ in the THz range, that is, for graphene doping densities $|n| \gg c/(\pi e \mu)$. This relation amounts to $|n| \gg 6.6 \times 10^{16}/\mu$, given in the units of cm^{-2} when the mobility μ is expressed in the units $\text{cm}^2/(\text{V s})$. Thus, the DPP damping may only be neglected in clean samples of graphene with large densities of charge carriers, e.g., $|n| \sim 10^{13} \text{ cm}^{-2}$ when $\mu \sim 10^5 \text{ cm}^2/(\text{V s})$.

We further show in Fig. 1 several level curves of the normalized total probability density $\bar{F} = F/F_c$, with $F_c = 4e^2/(\pi\omega_c^2 k_c)$, in the plane of reduced frequency and reduced wave number, $(\bar{\omega}, \bar{k})$, for the incident electron energy

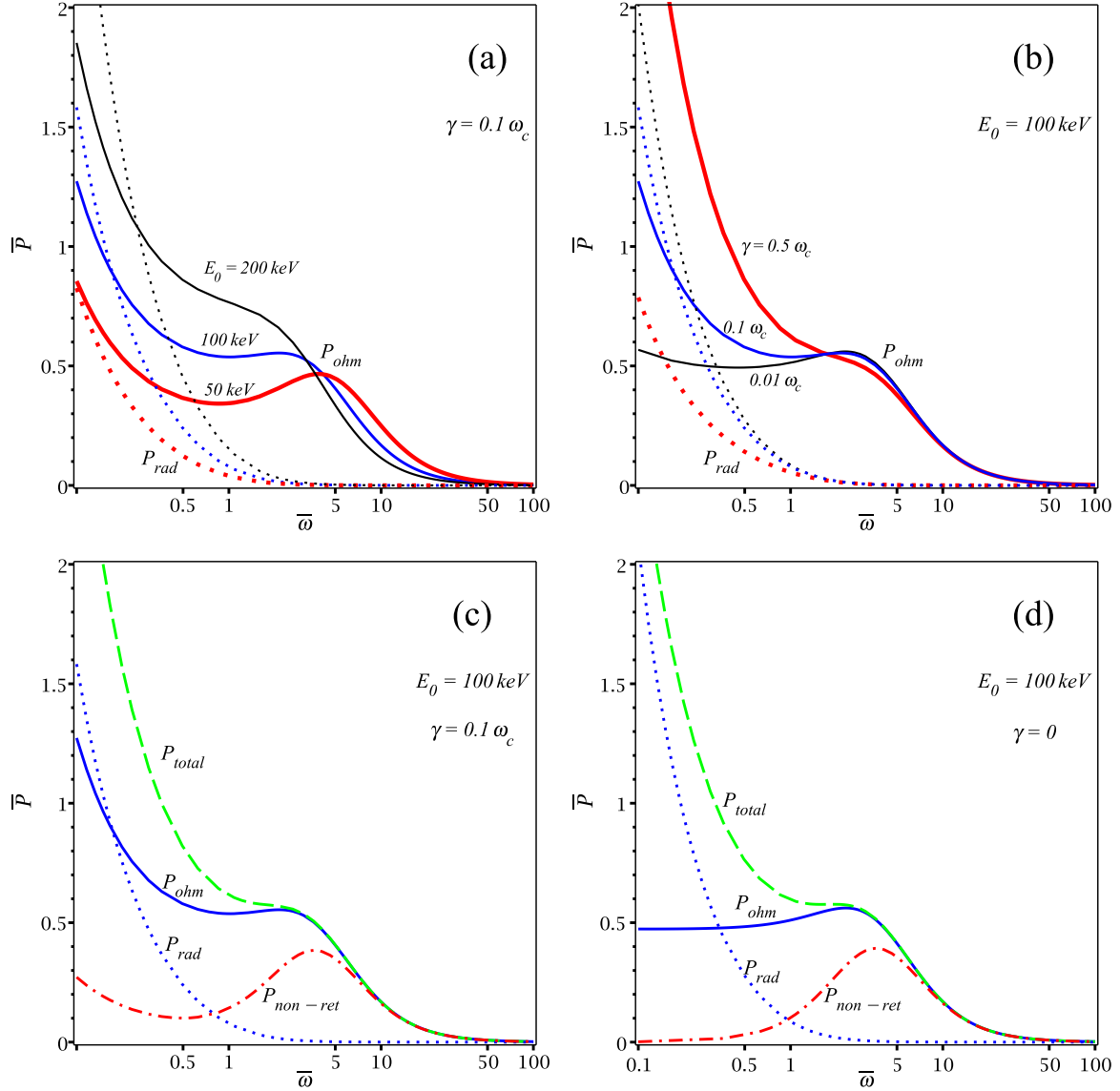


FIG. 3. Contributions to the integrated probability density \bar{P} for energy loss $\hbar\omega$ obtained from Eq. (36) with $k_s \rightarrow \infty$ for an electron with energy E_0 passing through a graphene layer described by the conductivity in Eq. (42). Results are shown for the reduced density $\bar{P} = \pi \varepsilon_F P/4$, where $\varepsilon_F = \hbar v_F k_F$, vs reduced frequency $\bar{\omega} = \omega/\omega_c$, where $\omega_c = k_F v_B v_F/c$, for contributions P_{ohm} due to the Joule energy (solid lines) using Eq. (34) and P_{rad} due to the radiated energy (dotted lines) using Eq. (35). In (a), three cases are shown for $E_0 = 50$ (thick red lines), 100 (medium blue lines), and 200 keV (thin black lines) with fixed $\gamma = 0.1\omega_c$, whereas in (b), three cases are shown for $\gamma = 0.01\omega_c$ (thin black lines), $\gamma = 0.1\omega_c$ (medium blue lines) and $0.5\omega_c$ (thick red lines) with fixed $E_0 = 100$ keV. In (c) and (d), besides the Joule contribution P_{ohm} (solid blue line) and the radiative contribution P_{rad} (dotted blue line) for $E_0 = 100$ keV, also shown are their sum $P_{total} = P_{ohm} + P_{rad}$ (dashed green line) and the probability density P_{nonret} in the nonretarded limit (dash-dotted red line) from Eq. (36) using Eq. (37) for (c) $\gamma = 0.1\omega_c$ and (d) 0.

$E_0 = 100$ keV and for three values of the damping rate in the range $\gamma \leq \omega_c$. One notices that the probability density spreads around the DPP dispersion curve, Eq. (45) in reduced units, most noticeably in the low k region. The spreading in the region below the light line, $\omega < ck$, is seen in Fig. 1 to increase with increasing γ , in accordance with the findings of Ref. [47]. However, unlike Ref. [47], we also observe in Fig. 1 a comparably large spreading in the region above the light line, $\omega > ck$, which seems to be rather independent from γ .

In order to elucidate the origins of this spreading, we plot in Fig. 2 the contributions of the Joule energy, F_{ohm}

from Eq. (34), and the radiated energy, F_{rad} from Eq. (35), to the total probability density F , shown as a function of frequency for several cross sections with fixed values of the wave number k . One notices that, for a sufficiently small damping rate, say $\gamma = 0.01\omega_c$, the Joule energy is represented by a resonant peak that follows closely the DPP dispersion relation in Eq. (45), which is quite narrow and produces negligible contribution above the light line. As the damping rate increases, the width of the DPP peak also increases in a rather asymmetric manner, with its high-energy tail extending well above the light dispersion $\omega = ck$. On the other hand, the contribution from radiation energy is always located above the

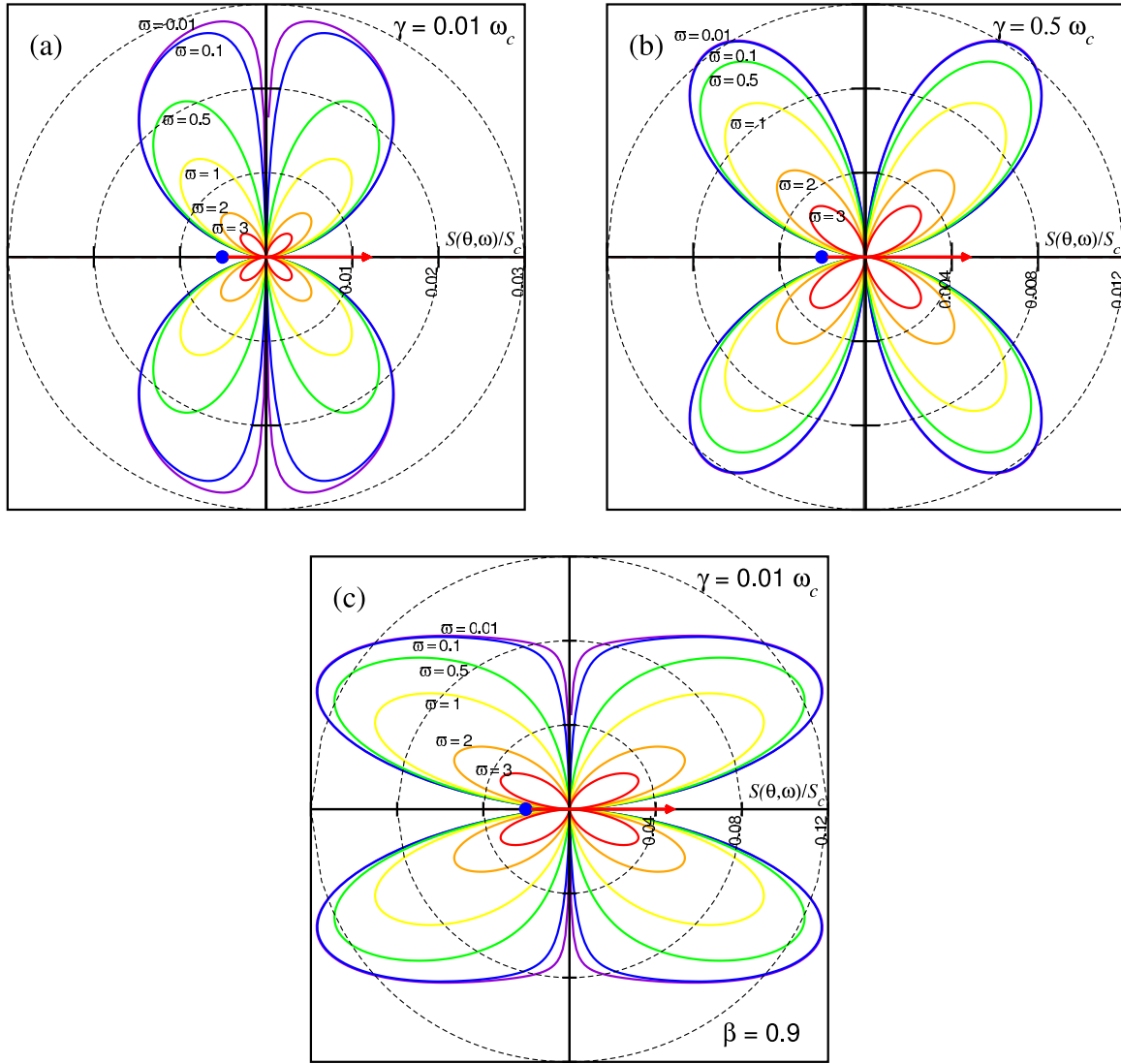


FIG. 4. Spectral density of the radiated energy S , Eq. (40), from a layer of doped graphene described by the Drude conductivity, Eq. (42), with damping rates (a) $\gamma = 0.01\omega_c$ and (b) $0.5\omega_c$ due to the passage of a 100 keV electron on a perpendicular trajectory. (c) same as (a) for the highly relativistic case with $\beta = 0.9$ (electron kinetic energy ≈ 660 keV). Results are shown for the reduced spectral density S/S_c where $S_c = e^2/c$ as a function of the emission angle θ relative to the electron trajectory in polar representation, and various values of the reduced frequency $\bar{\omega} = \omega/\omega_c$, where $\omega_c = k_F v_F/c$.

light line and is represented by a rather broad tail at frequencies $\omega > ck$, which is most pronounced for the vanishing damping, $\gamma = 0$, and only weakly decreases in magnitude, but not in the range, with increasing γ . Notice that the radiation contribution is particularly pronounced at lower values of k (and hence, lower ω), while it quickly becomes negligible as k increases.

As mentioned above, the EELS experiments often probe integrated probability density $P(\omega)$, Eq. (36), where one may take $k_s \rightarrow \infty$. In the case of radiated energy losses, this amounts to collecting the radiation emitted at fixed frequency ω over all directions,

$$P_{\text{rad}}(\omega) = \frac{1}{\omega} \iint d^2\hat{\Omega} S(\theta, \omega). \quad (46)$$

In Fig. 3, we show calculations of the Joule, P_{ohm} , and radiation, P_{rad} , contributions to the total density considering different values of γ and the incident electron energy E_0 .

We notice in panel (a) that both contributions increase with increasing E_0 for reduced frequencies $\bar{\omega} \lesssim 5$, while the reverse is true for the Joule contribution at higher frequencies. Panel (b) shows remarkably opposing trends, with the radiation contribution decreasing and the Joule contribution increasing with increasing γ . As a result, one notices surprisingly strong dependence of *relative* contributions of the Ohmic and radiation losses on the DPP damping. This is particularly important knowing that graphene samples may exhibit great range of variability in their mobility due to the presence of impurities and defects [32].

In panels (c) and (d), we further analyze the Ohmic and radiation contributions to energy losses and compare their sum, $P_{\text{total}} = P_{\text{ohm}} + P_{\text{rad}}$, with the integrated probability density in nonretarded limit, P_{nonret} . Given that the radiation contribution is absent in P_{nonret} , the large differences seen between P_{ohm} and P_{nonret} show that relativistic effects are important for the

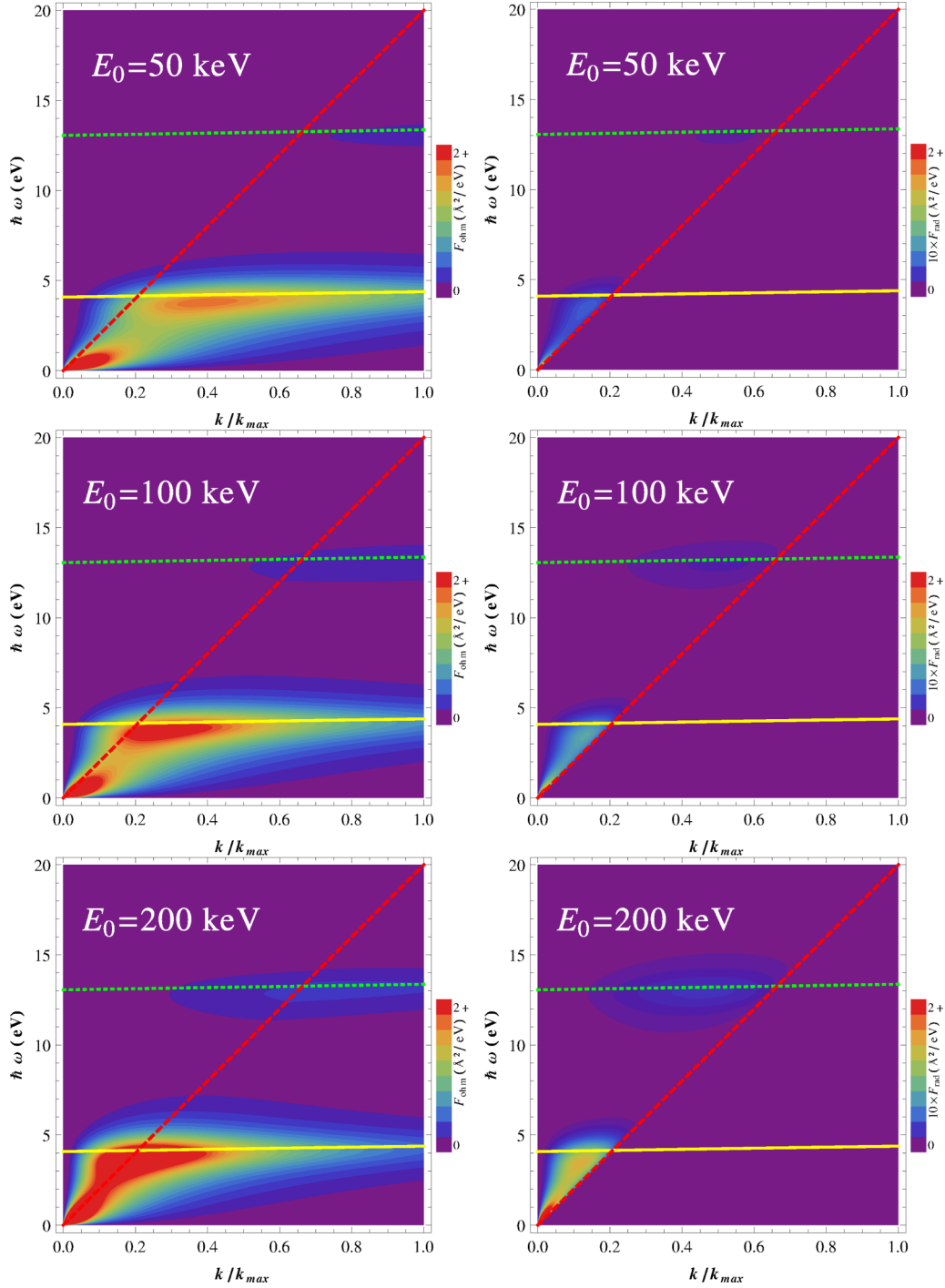


FIG. 5. Probability densities of the Joule energy loss F_{ohm} (left column) and the radiative energy loss F_{rad} (right column) obtained from Eqs. (34) and (35), respectively, using the Drude-Lorentz conductivity model of Eq. (44) with the π - and σ -electron density parameters given in the text. Results are shown as function of energy loss $\hbar\omega$ (in eV) and the relative momentum transfer k/k_{max} (with $k_{\text{max}} = 0.1 \text{ nm}^{-1}$) for an electron with different energies E_0 passing through a layer of graphene. The F -values are in units of $\text{Å}^2/\text{eV}$, and the radiative contribution is multiplied by a factor of 10 in order to make it visible at low incident energies. Also shown are the dispersion of light, $\hbar\omega = ck$ (dashed red line), as well as the nonrelativistic dispersion relations of the π (continuous yellow line) and $\pi + \sigma$ (dotted green line) plasmons for single layered graphene.

Joule energy losses at reduced frequencies $\bar{\omega} \lesssim 10$. This may be traced back, at least in the limit of weak damping, to large changes in the dispersion relation due to retardation effects seen in Fig. 1 (similar behavior has been observed also for

surface plasmons in metallic slabs [48]). To illustrate this point, we show in Fig. 3(d) analytical results for various contributions to the integrated density of energy losses in the case of $\gamma = 0$, which we label by a superscript (0). Specifically, one obtains

for Ohmic losses with retardation

$$P_{\text{ohm}}^{(0)}(\omega) = \frac{8\beta^2}{\varepsilon_F} \frac{\bar{\omega}^2 + 4}{(\beta^2\bar{\omega}^2 + 4)^2}, \quad (47)$$

which levels off at a constant value of $P_{\text{ohm}}^{(0)} \approx 2\beta^2/\varepsilon_F$ when $\bar{\omega} \lesssim 1$. On the other hand, energy losses in nonretarded limit for the case $\gamma = 0$, $P_{\text{nonret}}^{(0)}(\omega)$, are given by same expression as in Eq. (47), but with the numerator $\bar{\omega}^2 + 4$ replaced by $\bar{\omega}^2$, indicating a quadratic dependence $P_{\text{nonret}}^{(0)}(\omega) \approx \bar{\omega}^2\beta^2/(2\varepsilon_F)$ when $\bar{\omega} \ll 1$. At the same time, the contribution of the radiative energy losses in the case $\gamma = 0$ prevails at frequencies $\bar{\omega} \lesssim 0.5$, and is given by

$$P_{\text{rad}}^{(0)}(\omega) = \frac{4}{\pi\varepsilon_F} \frac{1}{\beta\bar{\omega}(\beta^2\bar{\omega}^2 + 4)^2} \left[(4 + 3\beta^2\bar{\omega}^2 + 4\beta^2 - \beta^4\bar{\omega}^2) \times \ln\left(\frac{1+\beta}{1-\beta}\right) - 2\beta(\beta^2\bar{\omega}^2 + 4) - 2\beta^3\bar{\omega}(\beta^2\bar{\omega}^2 + 4) \arctan\left(\frac{2}{\bar{\omega}}\right) \right]. \quad (48)$$

Even though the case $\gamma = 0$ is a theoretical idealization of an undamped DPP, one may conclude from the above analysis that sufficiently clean samples of graphene irradiated by the keV electrons under normal incidence may radiate quite effectively at the sub-THz frequencies.

While the features observed in Fig. 3 for P_{ohm} in the THz-frequency range are likely inaccessible in typical EEL spectra, the remarkable dependencies of the radiative energy loss P_{rad} on both the incident electron energy E_0 and the damping rate γ can possibly give rise to readily observable features in the angular distribution of the spectral density, $\mathcal{S}(\theta, \omega)$, of the energy radiated in that range of frequencies. Using the Drude conductivity from Eq. (42) in Eq. (40) we evaluate \mathcal{S} resulting from the passage of a 100 keV electron on a perpendicular trajectory through a layer of doped graphene with two damping rates γ . Figure 4 shows the angle-resolved distribution of the radiated energy in a polar plot in the form of level curves for several values of $\bar{\omega} = \omega/\omega_c$. We observe that, for the higher value of γ , the angular distributions are narrowly peaked around the directions $\pi/4$ and $3\pi/4$ for any value of ω considered, while, for the smaller γ , the radiation emitted at lower frequencies presents a marked spread towards the graphene plane. Also, we observe that the smaller the value of γ , the higher the density of radiated energy is, in agreement with what was observed in Fig. 3. In either case, the radiation is practically zero along the electron trajectory ($\theta = 0, \pi$). Nevertheless, when the kinetic energy of the electron is increased to highly-relativistic velocities [panel (c) in Fig. 4], the distribution spreads towards the direction of the incident electron's trajectory, though maintaining the emission pattern with respect to the surface (i.e., for small γ there is still a strong component parallel to the surface at low ω).

The narrow focusing of the angular distribution of radiated energy about the directions $\pi/4$ and $3\pi/4$ seen in Fig. 4(b) for the larger γ value may be ascribed to the first θ -dependent factor in Eq. (40). On the other hand, the distortion of the radiation lobes seen in Fig. 4(a) for a smaller γ value is clearly a signature of an increasingly well-defined DPP, which appears particularly strongly skewed towards the plane of graphene as

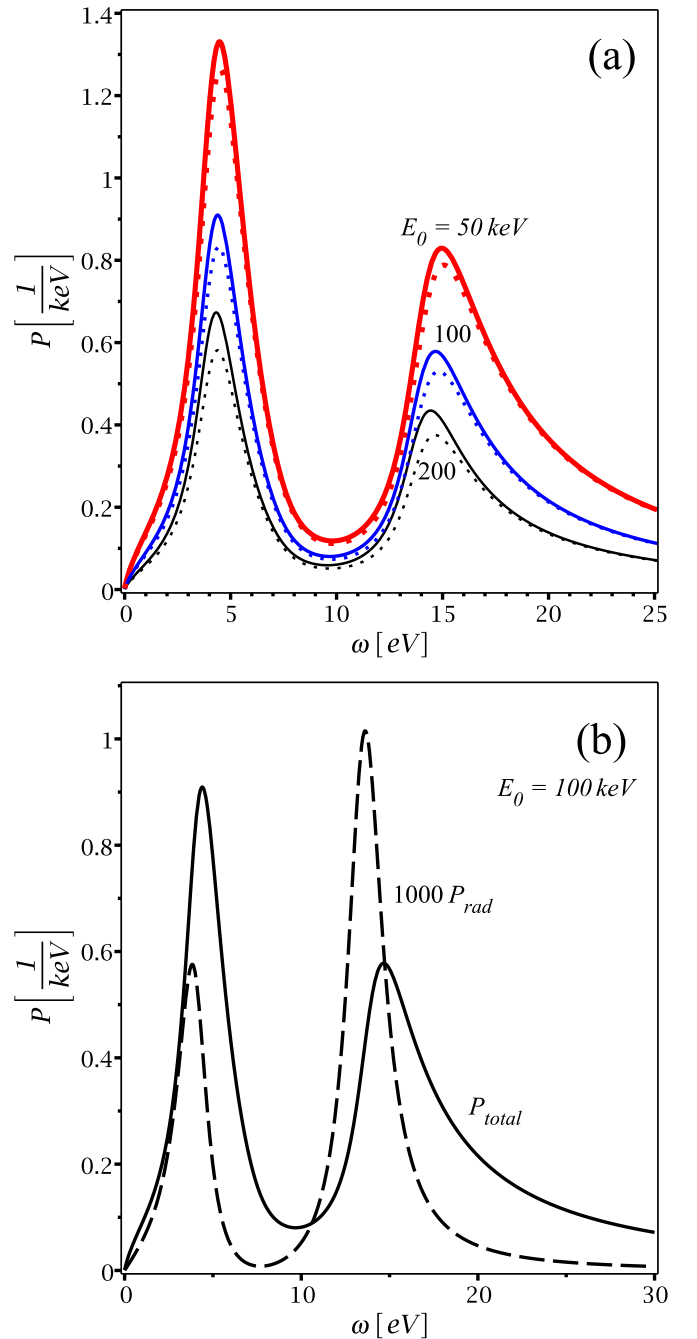


FIG. 6. Integrated probability density P from Eq. (36) vs energy loss $\hbar\omega$ of electrons with the kinetic energy E_0 , which are collected with their scattering angles up to $\vartheta = 20$ mrad after passing through a layer of graphene described by the Drude-Lorentz conductivity, Eq. (44). (a) shows results for the total P when the retardation effects are included (solid lines) by using Eqs. (34) and (35) and when they are neglected (dotted lines) by using Eq. (37) for $E_0 = 50$ (thick red lines), 100 (medium blue lines), and 200 (thin black lines). (b) reproduces the total probability density P_{total} from (a) in the case of $E_0 = 100$ keV (solid black line) and compares it with the contribution from the radiated energy P_{rad} (dashed black line), which is calculated from Eq. (36) by using Eq. (35) and is multiplied by a factor of 10^3 .

the frequency decreases. This feature may be accessible in an angle-resolved THz spectroscopy of the light radiated from graphene in a TEM.

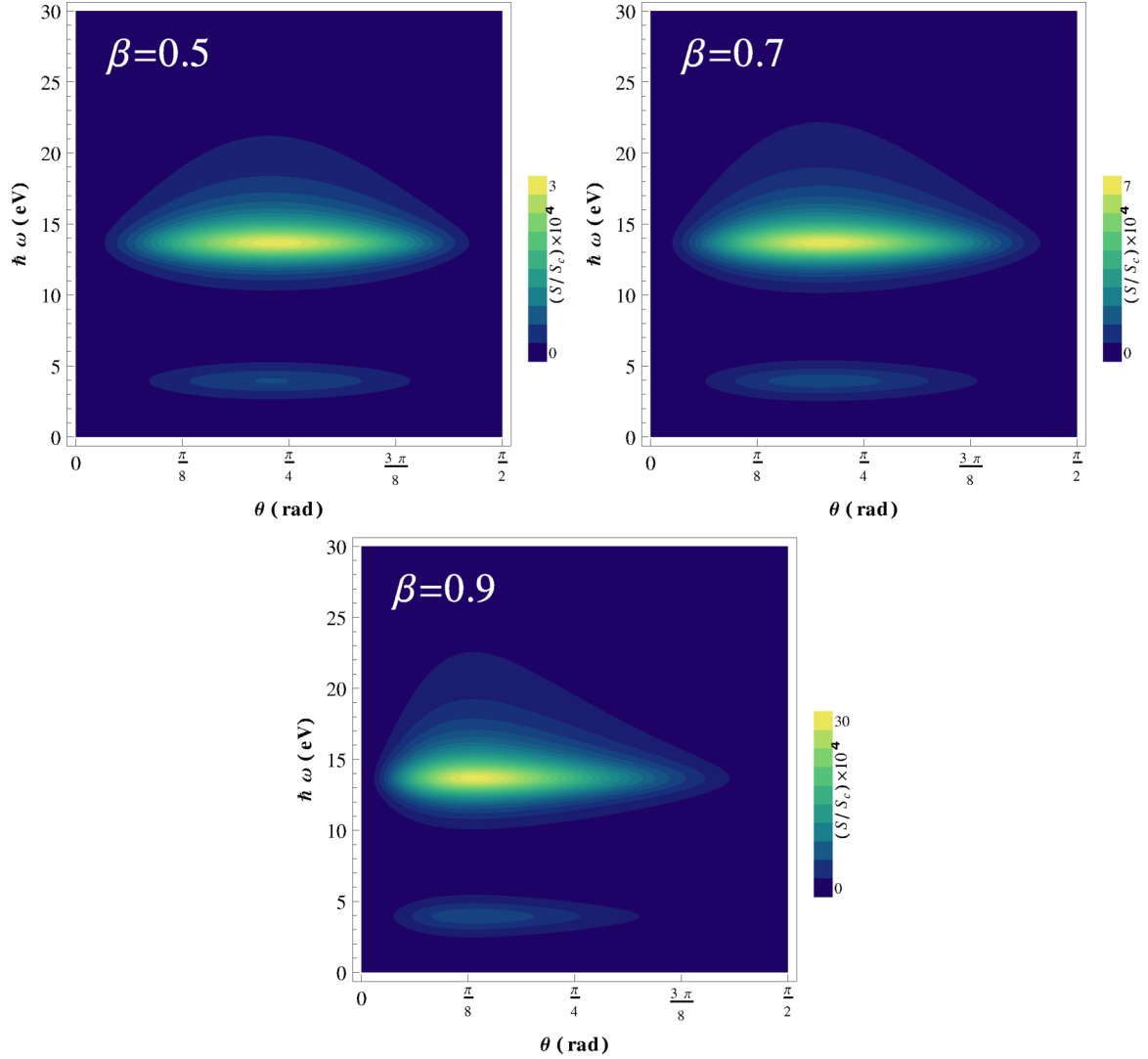


FIG. 7. Spectral density of the radiated energy S , Eq. (40), from a layer of graphene described by the Drude-Lorentz conductivity, Eq. (44), due to the passage of an electron on a perpendicular trajectory with various velocities $v = \beta c$. Results are shown for the reduced spectral density S/S_c where $S_c = e^2/c$ vs the emission angle θ relative to the electron trajectory and the frequency ω expressed in the units of electron energy loss [eV].

B. Visible-to-ultraviolet frequencies

We now focus on the higher-frequency range, in which the Drude-Lorentz conductivity model of Eq. (44) is more suitable for describing the dynamic polarization of both the π and σ electrons in graphene. In Fig. 5, we show the probability density F as a function of energy loss $\hbar\omega$ and the reduced momentum k/k_{\max} for electrons moving at different incident energies E_0 . The double-pole model of Eq. (44) gives rise to the features in F observed around 4 and 14 eV, corresponding to the well known π and $\pi + \sigma$ peaks [15,19,21]. It is remarkable that those peak structures in the probability density due to the Joule energy, F_{ohm} , extend well inside the light cone, $\omega > ck$, for increasing incident electron energy. This is a consequence of the relatively large peak widths γ_π and γ_σ of the π and σ electrons, which are fixed parameters of the model in Eq. (44). At the same time, the probability density due to the radiated energy F_{rad} also shows features corresponding to the π and $\pi + \sigma$ peaks, which are localized inside the light cone, $\omega > ck$, but

appear to have a magnitude that is suppressed in comparison to the same features in the Joule energy loss.

In Fig. 6, we show the integrated probability density for energy loss P using the electron scattering angle of $\vartheta = 20$ mrad, which corresponds to a EELS experiment [15]. With the model in Eq. (44), the experimental π and $\pi + \sigma$ peaks at around 4 and 14 eV are satisfactorily reproduced [15,19]. In Fig. 6(a), we compare the total integrated density P_{total} with its nonretarded limit for several incident electron energies E_0 , while in Fig. 6(b), we compare P_{total} with the integrated density P_{rad} due to the radiated energy for $E_0 = 100$ keV. The most remarkable fact shown here is the relevance of including the retardation effects in the calculation of energy loss spectra when the incident electron energy in EELS increases. This is especially true in the regions around the main peaks in P_{total} , with their heights being increased by more than 10% when the retardation effects are included, as shown in Fig. 6(a). On the other hand, in contrast to the low-frequency regime (Fig. 3), Fig. 6(b) shows that the radiative term P_{rad} yields a very low

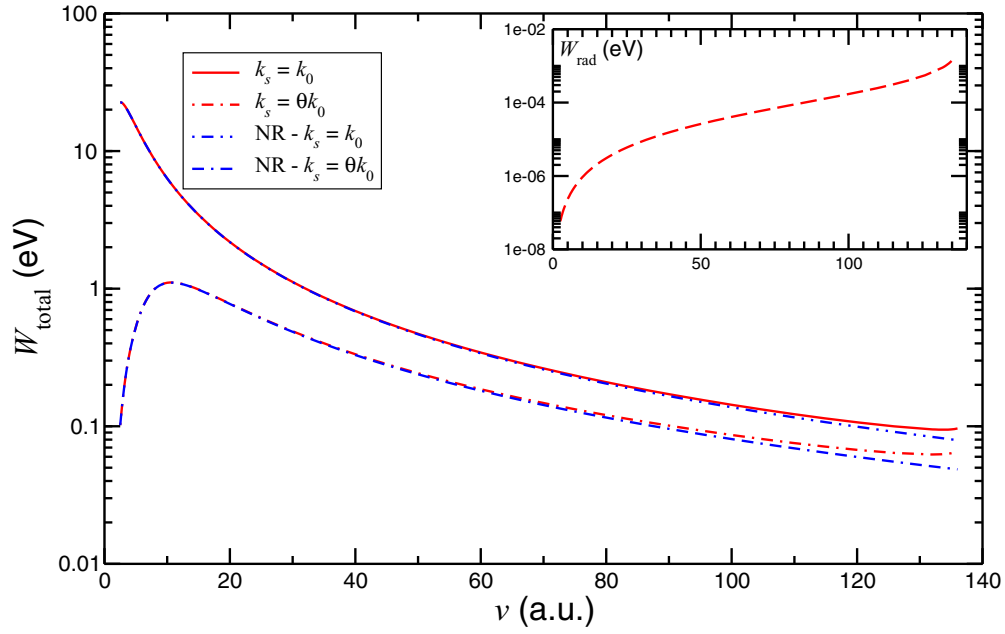


FIG. 8. The total integrated energy loss $W_{\text{total}} = W_{\text{ohm}} + W_{\text{rad}}$ from Eqs. (32) and (33) for an electron on a perpendicular trajectory as a function of its speed v (in atomic units). Two values are considered for the k integration limit: $k_s = k_0$ (red, continuous line) and the restricted case $k_s = \vartheta k_0$ (red, dash-dotted line) with $\vartheta = 20$ mrad. Also included are calculations for the nonretarded limit, Eq. (37), with $k_s = k_0$ (blue, dash-double dotted line) and $k_s = \vartheta k_0$ (blue, dash-dotted line). Inset: radiative contribution W_{rad} .

overall contribution to the total probability density, which is accordingly dominated by the Joule energy losses, P_{ohm} , in the range of visible to UV frequencies. Interestingly, the peak positions in P_{rad} in Fig. 6(b) are seen to be red shifted compared to those in P_{total} .

The angular distribution of the radiated energy $\mathcal{S}(\theta, \omega)$ [Eq. (40)] for the visible to UV range of frequencies presents the same general trend than that for the THz range, but now with the two characteristic peaks at ≈ 4 and ≈ 14 eV instead of the monotonic decrease of \mathcal{S} with ω ; for the fixed values of γ_v used here, it presents a preferential direction around $\pi/4$ at the moderately relativistic energies typical in a TEM, $E_0 \approx 100$ keV. Again, when the incident energy increases to ultrarelativistic velocities, the peaks of emitted radiation pattern skew towards the direction of incidence while increasing the intensity. These features are illustrated in Fig. 7 for increasing values of β , from $\beta = 0.5$ (corresponding to an energy $E_0 \approx 80$ keV) to $\beta = 0.9$ ($E_0 \approx 660$ keV). (We do not show distribution in the half-space below graphene, with $\pi/2 < \theta < \pi$, which is equal but symmetrically placed relative to graphene.) As mentioned for the low-frequency range, the spectral density is dominated by the first-angle dependent factor in Eq. (40). Notice that in the present range of frequencies there is very little dispersion in angle. This may be related to the fact that, unlike the Dirac plasmon at low frequencies, the peaks in the high-frequency response of graphene do not show a collective, or resonant, character in the optical limit, but are rather found to be pure interband single-particle transitions of the type $\pi \rightarrow \pi^*$ and $\sigma \rightarrow \sigma^*$ [21,44,45]. Thus no significant dispersion with angle is observed in Fig. 7 using the local model of Eq. (44). However, this picture may be changed if nonlocal effects are included in the form of a wave number dependent conductivity, $\sigma(k, \omega)$,

because the $\pi \rightarrow \pi^*$ and $\sigma \rightarrow \sigma^*$ transitions were shown to suddenly acquire a collective character as k increases. With $k = \frac{\omega}{c} \sin \theta$ this could result in an observable skewing of the angular distribution in $\mathcal{S}(\theta, \omega)$ towards the plane of graphene at high frequencies, similar to that seen in Fig. 4(a) for the THz frequencies [45].

Finally, it is interesting to study the total energy lost by a charged particle due to the Joule and radiation contributions, obtained from Eqs. (32) and (33), respectively. In Fig. 8, we show the energy lost by an electron crossing the graphene layer as a function of its speed. In particular, we consider the results for $k_s = k_0$, corresponding to the case of an hemispherical detector collecting the electrons scattered between 0 and $\pi/2$ (red, continuous line), and a restricted case with $k_s = \theta k_0$, where $\theta = 20$ mrad (red, dash-dotted line). This restriction is seen in Fig. 8 to only affect the Joule contribution. We also include in Fig. 8 results in the nonretarded limit from Eq. (37), which only display noticeable effects at very large electron speeds. On the other hand, the radiative contribution (shown in the inset) is almost negligible except for very large speeds, close to the limit $v \rightarrow c$. This feature points to a possibility to design detectors for relativistic particles based on TR from multilayer graphene, or graphite [49].

The results in Fig. 8 show that the total energy loss of a 100 keV electron is on the order of 1 eV, whereas its deflection angle is well below ~ 10 mrad, thereby justifying our initial assumption that the incident electron velocity is constant.

IV. CONCLUSIONS

We present a completely relativistic formulation for the energy loss of a charged particle traversing a conductive monoatomic layer. The theory is applied to the case of

graphene in a transmission electron microscope (TEM) using two models of conductivity appropriate for different frequency regimes: (a) THz-frequency range and (b) optical range. We concentrated in these two specific ranges because graphene shows remarkable properties in both regimes, making it suitable for applications in devices, nanocomposites, and electronic nanofillers. We distinguish two types of contributions to the electron energy loss: the energy deposited in the graphene sheet in the form of electronic excitations (Ohm losses), and the energy that is emitted in the form of radiation. The properties of each contribution are described in terms of analytical methods. For both contributions we apply them to illustrative examples, showing the angular distribution of the emitted radiation, as well as the spectral distribution in the (k, ω) plane. We also discuss the energy loss densities for both contributions considering the cases of a detector with a restricted angular acceptance, as well as the integration over all the electron momentum transfers to graphene.

In the THz-frequency range, where the dynamic response of doped graphene is dominated by its Dirac plasmon polariton (DPP), we find that the Ohmic and radiative contributions are comparable in magnitude, while showing distinctive features in both their momentum (angular) and energy distributions. We find that interplay between the two contributions is strongly affected by the damping rate of the DPP. For a well defined DPP, when the damping is low, we find a localized peak in the Ohmic energy loss that is located outside the light cone, whereas the radiated energy is broadly distributed and it extends always within the light cone. Moreover, the angular distribution of the emitted radiation in the THz range gets skewed towards the plane of graphene when the damping rate decreases. This effect of damping in graphene may be experimentally observable in angle-resolved measurements of the radiated spectra at the sub-THz range in TEM. On the other hand, the momentum integrated energy loss density due to Ohmic contribution shows strong relativistic effects when compared to the results obtained with retardation effects neglected. Overall, our analysis shows that incident electrons with energies ~ 100 keV can excite the DPP in doped graphene quite effectively, while providing an efficient source of sub-THz radiation with a broad energy spectrum and characteristically skewed angular distribution.

In the optical range of frequencies, where graphene's dynamic response is dominated by the $\pi \rightarrow \pi^*$ and $\sigma \rightarrow \sigma^*$ interband electron transitions, we find that the contribution due to emitted radiation is heavily suppressed when compared to the Ohmic losses. For the latter type of losses, we observe a displacement of the characteristic π and $\pi + \sigma$ peaks in the spectra towards the lower k values (i.e., longer wavelengths) as the energy of the incident particle increases, falling inside the light cone at relativistic electron energies. As a consequence, the momentum integrated energy loss density, which is dominated by the Ohmic losses, is found to exhibit a 10% increase in the characteristic peak heights due to relativistic effects. This role of relativistic effects may be experimentally observable in the TEM energy loss spectra. At the same time, the integrated energy loss density due to emitted radiation also displays the π and $\pi + \sigma$ peaks, which are red shifted in comparison to those in the Ohmic losses. The total radiative losses turn out to be several orders of magnitude lower than

the nonradiative ones, showing a very steep increase when the speed of the incident particle approaches the speed of light. This increase may be of interest for designing graphene based detectors for measuring the Lorentz factors of energetic particles with transition radiation [50].

ACKNOWLEDGMENTS

This work has been supported partly by CONICET (PIP 11220120100374) and ANPCyT (PICT 2012-1163) from Argentina. Z.L.M. gratefully acknowledges CONICET for funding a travel fellowship, and Natural Science and Engineering Research Council of Canada (Grant No. 249506-2011) of Canada for financial support.

APPENDIX A: RETARDED GREEN'S FUNCTION FOR LAYERED STRUCTURE

We consider Eq. (4) of the main text and write it in the time domain as scalar wave equation for each component $\psi(\mathbf{R}, t)$ of the Hertz vector $\mathbf{\Pi}(\mathbf{R}, t)$,

$$\left(\nabla^2 - \frac{1}{c^2} \frac{\partial^2}{\partial t^2}\right) \psi(\mathbf{R}, t) = -4\pi f(\mathbf{R}, t), \quad (\text{A1})$$

where $f(\mathbf{R}, t)$ is a nonhomogeneous term due to the corresponding component of the current density $\mathbf{J}(\mathbf{R}, t)$. A solution of the above equation due to the nonhomogeneous term is given by

$$\psi(\mathbf{R}, t) = \iiint d^3\mathbf{R}' \int_{-\infty}^{\infty} dt' G(\mathbf{R} - \mathbf{R}', t - t') f(\mathbf{R}', t'), \quad (\text{A2})$$

where the retarded Green's function is given by [33]

$$G(\mathbf{R}, t) = \frac{1}{R} \delta\left(\frac{R}{c} - t\right) = \int_{-\infty}^{\infty} \frac{d\omega}{2\pi} e^{-i\omega t} \frac{1}{R} e^{i\frac{\omega}{c}R}, \quad (\text{A3})$$

with $R = \|\mathbf{R}\| = \sqrt{r^2 + z^2}$ and $r = \|\mathbf{r}\|$. Hence performing the Fourier transform of $G(\mathbf{R}, t)$ with respect to time and the coordinates $\mathbf{r} = \{x, y\}$ gives an expression for the Green's function as

$$\begin{aligned} G(\mathbf{k}, z, \omega) &= \iint d^2\mathbf{r} \int_{-\infty}^{\infty} dt e^{-i\mathbf{k}\cdot\mathbf{r} + i\omega t} G(\mathbf{R}, t) \\ &= 2\pi \int_0^{\infty} \frac{dr r}{\sqrt{r^2 + z^2}} J_0(kr) e^{i\frac{\omega}{c}\sqrt{r^2 + z^2}}, \quad (\text{A4}) \end{aligned}$$

where $k = \|\mathbf{k}\|$ and J_0 is the Bessel function of the first kind of zeroth order. It is important to notice that the real and imaginary parts of the last expression in Eq. (A4) are even and odd functions of ω , respectively. Using the table integrals 8 and 9 from section 2.12.23 in Ref. [51] gives a result for the retarded Green's function listed in Eqs. (6), (7), and (8) of the main text, which is valid for both positive and negative frequencies.

APPENDIX B: JOULE ENERGY AND TRANSITION RADIATION

We first evaluate the Joule energy as the work done by the total electric field on the induced charge current density in the

conducting layer,

$$\begin{aligned}
 W_{\text{ohm}} &= \int_{-\infty}^{\infty} dt \iiint d^3\mathbf{R} \mathbf{J}_{\text{ind}}(\mathbf{R}, t) \cdot \mathbf{E}(\mathbf{R}, t) \\
 &= \iint d^2\mathbf{r} \int_{-\infty}^{\infty} dt \mathbf{j}(\mathbf{r}, t) \cdot \mathbf{E}_{\parallel}(\mathbf{r}, 0, t) \\
 &= \iint \frac{d^2\mathbf{k}}{(2\pi)^2} \int_{-\infty}^{\infty} \frac{d\omega}{2\pi} \mathbf{j}(\mathbf{k}, \omega) \cdot \mathbf{E}_{\parallel}(-\mathbf{k}, 0, -\omega) \\
 &= \iint \frac{d^2\mathbf{k}}{(2\pi)^2} \int_{-\infty}^{\infty} \frac{d\omega}{2\pi} \sigma(k, \omega) |\mathbf{E}_{\parallel}(\mathbf{k}, 0, \omega)|^2 \\
 &= \frac{(Ze)^2}{\pi v^2} \iint \frac{d^2\mathbf{k}}{(2\pi)^2} \int_0^{\infty} d\omega \frac{(kA)^2}{\left|1 + \frac{2\pi}{\omega} \kappa \sigma(k, \omega)\right|^2} \\
 &\quad \times \Re[\sigma(k, \omega)], \tag{B1}
 \end{aligned}$$

where we have used Eqs. (12), (13), and (20). The ω integral in the last line of Eq. (B1) may be decomposed to give Eq. (32) of the main text, which proves that when the two terms with $\Re[\sigma]$ in Eq. (29) are used in Eq. (28) for W_{ext} , one indeed obtains $-W_{\text{ohm}}$. Moreover, the result in Eq. (32) demonstrates that the Ohmic heating of the conducting layer may occur both inside and outside the light cone, defined by $\omega = ck$, as long as various scattering processes undergone by the charge carriers in that layer give rise to finite $\Re[\sigma]$ in those domains of the (ω, k) plane. We note that Eq. (B1) describes the energy that remains localized in the graphene layer and eventually dissipates in the form of Ohmic heat owing to various decay mechanisms for electronic excitations brought up by the incident particle.

We next evaluate the total electromagnetic energy radiated in the far field from the flux of Poynting vector due to induced electric and magnetic fields taken over a large surface S enclosing the conducting layer,

$$\begin{aligned}
 W_{\text{rad}} &= \frac{c}{4\pi} \int_{-\infty}^{\infty} dt \oint_S dS \hat{\mathbf{n}} \cdot [\mathbf{E}_{\text{ind}}(\mathbf{R}, t) \times \mathbf{H}_{\text{ind}}(\mathbf{R}, t)] \\
 &= \frac{c}{4\pi} \oint_S dS \hat{\mathbf{n}} \cdot \int_{-\infty}^{\infty} \frac{d\omega}{2\pi} [\mathbf{E}_{\text{ind}}(\mathbf{R}, \omega) \times \mathbf{H}_{\text{ind}}(\mathbf{R}, -\omega)] \\
 &= \frac{c}{(2\pi)^2} \int_0^{\infty} d\omega \Re \oint_S dS \hat{\mathbf{n}} \cdot [\mathbf{E}_{\text{ind}}(\mathbf{R}, \omega) \times \mathbf{H}_{\text{ind}}^*(\mathbf{R}, \omega)], \tag{B2}
 \end{aligned}$$

where $\hat{\mathbf{n}}$ is a unit outer normal vector on S . One possibility for the choice of the surface S is to take two planes at large distances from the conducting layer, $z = \pm\infty$ [35]. Then,

$dS = d^2\mathbf{r}$ and $\hat{\mathbf{n}} = \pm\hat{\mathbf{z}}$ on the two planes, so that there are two contributions to the surface integral in Eq. (B2), giving $W_{\text{rad}} = W_{\text{rad}}^> + W_{\text{rad}}^<$, with

$$\begin{aligned}
 W_{\text{rad}}^{\gtrless} &= \pm \frac{c}{(2\pi)^2} \lim_{z \rightarrow \pm\infty} \int_0^{\infty} d\omega \Re \iint \frac{d^2\mathbf{k}}{(2\pi)^2} \hat{\mathbf{z}} \cdot \\
 &\quad \times [\mathbf{E}_{\text{ind}}(\mathbf{k}, z, \omega) \times \mathbf{H}_{\text{ind}}^*(\mathbf{k}, z, \omega)]. \tag{B3}
 \end{aligned}$$

Using Eqs. (22) and (23) one finds that, when $\omega > ck$, the Poynting vector is given for arbitrary z by

$$\begin{aligned}
 &\mathbf{E}_{\text{ind}}(\mathbf{k}, z, \omega) \times \mathbf{H}_{\text{ind}}^*(\mathbf{k}, z, \omega) \\
 &= [\mathbf{k} + \hat{\mathbf{z}}\kappa \text{sign}(z)] \frac{\omega}{c} \left| k \frac{Ze}{v} \frac{A}{\omega} \frac{2\pi\sigma}{1 + \frac{2\pi}{\omega} \kappa \sigma} \right|^2, \tag{B4}
 \end{aligned}$$

whereas when $\omega < ck$, the Poynting vector vanishes for $z \rightarrow \pm\infty$ owing to the transformation of the exponential functions indicated in Eq. (24). Hence, using Eq. (B4) in Eq. (B3) gives $W_{\text{rad}}^> = W_{\text{rad}}^<$, so that the total radiated energy is given in Eq. (33) of the main text. This result proves that when the term with $|\sigma|^2$ in Eq. (29) is used in Eq. (28) for W_{ext} , one indeed obtains $-W_{\text{rad}}$.

We finally note that the expression in Eq. (40) of the main text for spectral density and angular distribution of the radiated energy may be obtained from an expression for the Poynting vector in terms of spherical waves in the far region based on asymptotic analysis due to Weyl [36,37]. Namely, it may be shown that, when the radial distance from the coordinate origin $R \rightarrow \infty$, the asymptotic form of the induced electric and magnetic fields in spherical coordinates are given by

$$\mathbf{E}_{\infty}(\mathbf{R}, \omega) \sim \frac{\kappa}{2\pi i} \mathbf{E}_{\text{ind}}(\mathbf{k}, 0, \omega) \frac{e^{i\frac{\omega}{c}R}}{R}, \tag{B5}$$

$$\mathbf{H}_{\infty}(\mathbf{R}, \omega) \sim \frac{\kappa}{2\pi i} \mathbf{H}_{\text{ind}}(\mathbf{k}, 0, \omega) \frac{e^{i\frac{\omega}{c}R}}{R}, \tag{B6}$$

where the in-plane Fourier transforms of the electric and magnetic fields, $\mathbf{E}_{\text{ind}}(\mathbf{k}, 0, \omega)$ and $\mathbf{H}_{\text{ind}}(\mathbf{k}, 0, \omega)$, are to be taken in the plane of graphene, $z = 0$. By replacing $\mathbf{k} = \{k_x, k_y\} = \frac{\omega}{c} \sin\theta \{\cos\varphi, \sin\varphi\}$ and $\kappa = \frac{\omega}{c} |\cos\theta|$, one can see that the factor $[\mathbf{k} + \hat{\mathbf{z}}\kappa \text{sgn}(z)]$ in Eq. (B4) becomes $\frac{\omega}{c} \hat{\mathbf{n}}$, where $\hat{\mathbf{n}} = \mathbf{R}/R$ is a unit normal vector on the surface of a large sphere S of radius R . Using Eqs. (B5) and (B6) in the last line of Eq. (B2) and writing $dS = R^2 d^2\hat{\Omega}$, immediately shows that the radiated energy in the upper hemisphere is given by Eq. (40) with a similar expression for the energy radiated in the lower hemisphere.

-
- [1] S. Stankovich, D. A. Dikin, G. H. B. Dommett, K. M. Kohlhaas, E. J. Zimney, E. A. Stach, R. D. Piner, S. T. Nguyen, and R. S. Ruoff, *Nature (London)* **442**, 282 (2006).
 [2] K. S. Novoselov, D. Jiang, F. Schedin, T. J. Booth, V. V. Khotkevich, S. V. Morozov, and A. K. Geim, *Proc. Natl. Acad. Sci. USA* **102**, 10451 (2005); K. S. Novoselov, A. K. Geim, S. V. Morozov, D. Jiang, M. I. Katsnelson, I. V. Grigorieva, and S. V. Dubonos, and A. A. Firsov, *Nature (London)* **438**, 197 (2005).
 [3] *Graphene Science Handbook* (Six-Volume Set), edited by

- Mahmood Aliofkhazraei, Nasar Ali, William I. Milne, Cengiz S. Ozkan, Stanislaw Mitura, and Juana L. Gervasoni (CRC Press, Taylor & Francis Inc., Boca Raton, 2016).
 [4] P. Blake, P. D. Brimicombe, R. R. Nair, T. J. Booth, D. Jiang, F. Schedin, L. A. Ponomarenko, S. V. Morozov, H. F. Gleeson, E. W. Hill, A. K. Geim, and K. S. Novoselov, *Nano Lett.* **8**, 1704 (2008).
 [5] R. R. Nair, P. Blake, A. N. Grigorenko, K. S. Novoselov, T. J. Booth, T. Stauber, N. M. R. Peres, and A. K. Geim, *Science* **320**, 1308 (2008).

- [6] T. J. Booth, P. Blake, R. R. Nair, D. Jiang, E. W. Hill, U. Bangert, A. Bleloch, M. Gass, K. S. Novoselov, and M. I. Katsnelson, and A. K. Geim, *Nano Lett.* **8**, 2442 (2008).
- [7] A. H. Castro Neto, F. Guinea, N. M. R. Peres, and K. S. Novoselov, and A. K. Geim, *Rev. Mod. Phys.* **81**, 109 (2009).
- [8] R. D. Dreyer, S. Park, C. W. Bielawski, and R. S. Ruoff, *Chem. Soc. Rev.* **39**, 228 (2010).
- [9] C. Lee, X. Wei, J. W. Kysar, and J. Hone, *Science* **321**, 385 (2008).
- [10] G. Wang, J. Yang, J. Park, X. Gou, B. Wang, H. Liu, and J. Yao, *J. Phys. Chem. C* **112**, 8192 (2008).
- [11] F. Xia, H. Wang, D. Xiao, M. Dubey, and A. Ramasubramaniam, *Nat. Photon.* **8**, 899 (2014).
- [12] F. Bonaccorso, Z. Sun, T. Hasan, and A. C. Ferrari, *Nat. Photon.* **4**, 611 (2010).
- [13] F. J. García de Abajo, *ACS Photon.* **1**, 135 (2014); A. N. Grigorenko, M. Polini, and K. S. Novoselov, *Nat. Photon.* **6**, 749 (2012).
- [14] S. Xiao, X. Zhu, B.-H. Li, and N. A. Mortensen, *Front. Phys.* **11**, 117801 (2016).
- [15] T. Eberlein, U. Bangert, R. R. Nair, R. Jones, M. Gass, A. L. Bleloch, K. S. Novoselov, A. Geim, and P. R. Briddon, *Phys. Rev. B* **77**, 233406 (2008).
- [16] F. Carbone, B. Barwick, O.-H. Kwon, H. S. Park, and J. S. Baskin, A. H. Zewail, *Chem. Phys. Lett.* **468**, 107 (2009).
- [17] P. Wachsmuth, R. Hambach, M. K. Kinyanjui, M. Guzzo, G. Benner, and U. Kaiser, *Phys. Rev. B* **88**, 075433 (2013).
- [18] M. D. Kapetanakis, W. Zhou, M. P. Oxley, J. Lee, M. P. Prange, S. J. Pennycook, J. C. Idrobo, and S. T. Pantelides, *Phys. Rev. B* **92**, 125147 (2015).
- [19] V. B. Jovanovic, I. Radovic, D. Borka, and Z. L. Miskovic, *Phys. Rev. B* **84**, 155416 (2011).
- [20] V. Despoja, D. Novko, K. Dekanic, M. Sunjic, and L. Marusic, *Phys. Rev. B* **87**, 075447 (2013).
- [21] F. J. Nelson, J.-C. Idrobo, J. D. Fite, Z. L. Miskovic, S. J. Pennycook, S. T. Pantelides, J. U. Lee, and A. C. Diebold, *Nano Lett.* **14**, 3827 (2014).
- [22] T. Ochiai, *J. Phys. Soc. Jpn.* **83**, 054705 (2014).
- [23] T. Zhan, D. Han, X. Hu, X. Liu, S.-T. Chui, and J. Zi, *Phys. Rev. B* **89**, 245434 (2014).
- [24] T. Zhao, S. Gong, M. Hu, R. Zhong, D. Liu, X. Chen, P. Zhang, X. Wang, C. Zhang, P. Wu, and S. Liu, *Scientific Reports* **5**, 16059 (2015).
- [25] L. J. Wong, I. Kaminer, O. Ilic, J. D. Joannopoulos, and M. Soljacic, *Nature Photonics* **10**, 46 (2016).
- [26] F. J. García de Abajo, *Rev. Mod. Phys.* **82**, 209 (2010).
- [27] T. Coenen, B. J. M. Brenny, E. J. Vesseur, and A. Polman, *MRS Bull.* **40**, 359 (2015).
- [28] J. A. Stratton, *Electromagnetic Theory* (McGraw-Hill, New York, 1941).
- [29] J. Lindhard, K. Dan. Vidensk. Selsk., Mat.-Fys. Medd. **28**, 8 (1954).
- [30] Kenneth W.-K. Shung, *Phys. Rev. B* **34**, 979 (1986).
- [31] B. Wunsch, T. Stauber, F. Sols, and F. Guinea, *New J. Phys.* **8**, 318 (2006).
- [32] E. H. Hwang and S. Das Sarma, *Phys. Rev. B* **75**, 205418 (2007).
- [33] J. D. Jackson, *Classical Electrodynamics*, 2nd ed. (Wiley, New York, 1975).
- [34] V. L. Ginzburg and V. N. Tsytovich, *Transition Radiation and Transition Scattering* (Adam Hilger, Bristol, 1990).
- [35] M. I. Ryazanov, *Electrodynamics of Condensed Media* (Nauka, Moscow, 1984) (in Russian).
- [36] H. Weyl, *Ann. Phys.* **60**, 481 (1919).
- [37] L. Mandel and E. Wolf, *Optical Coherence and Quantum Optics* (Cambridge University Press, New York, 1995), Sec. 3.2.2.
- [38] A. Nemilentsau, T. Low, and G. Hanson, *Phys. Rev. Lett.* **116**, 066804 (2016).
- [39] D. Novko, M. Sunjic, and V. Despoja, *Phys. Rev. B* **93**, 125413 (2016).
- [40] A. L. Fetter, *Ann. Phys.* **88**, 1 (1974).
- [41] S. Das Sarma, S. Adam, E. H. Hwang, and E. Rossi, *Rev. Mod. Phys.* **83**, 407 (2011).
- [42] Z. Fei, A. S. Rodin, G. O. Andreev, W. Bao, A. S. McLeod, M. Wagner, L. M. Zhang, Z. Zhao, M. Thiemens, G. Dominguez, M. M. Fogler, A. H. Castro Neto, C. N. Lau, F. Keilmann, and D. N. Basov, *Nature (London)* **487**, 82 (2012).
- [43] Yu. V. Bludov, A. Ferreira, N. M. R. Peres, and M. I. Vasilevskiy, *Int. J. Mod. Phys. B* **27**, 1341001 (2013).
- [44] A. G. Marinopoulos, L. Reining, A. Rubio, and V. Olevano, *Phys. Rev. B* **69**, 245419 (2004).
- [45] D. Novko, V. Despoja, and M. Sunjic, *Phys. Rev. B* **91**, 195407 (2015).
- [46] K. A. Lyon., Z. L. Mišković, A. C. Diebold, and J.-C. Idrobo, *AIP Conf. Proc.* **1590**, 158 (2014).
- [47] H.-Y. Deng and K. Wakabayashi, *Phys. Rev. B* **92**, 045434 (2015).
- [48] R. H. Ritchie, *Surf. Sci.* **34**, 1 (1973).
- [49] A. Andronic and J. P. Wessels, *Nucl. Instrum. Methods A* **666**, 130 (2012).
- [50] M. L. Cherry, *Nucl. Instrum. Methods A* **706**, 39 (2013).
- [51] A. P. Prudnikov, Yu. A. Brychkov, and O. I. Marichev *Integrals and Series: Special Functions, Vol. 2* (Nauka, Moscow, 1983) (in Russian).